

ALMA MATER STUDIORUM - UNIVERSITÀ DI BOLOGNA

SCUOLA DI SCIENZE
DIPARTIMENTO DI FISICA E ASTRONOMIA

CORSO DI LAUREA IN ASTROFISICA E COSMOLOGIA

Kinematics modelling of molecular gas in NGC 3100

TESI DI LAUREA MAGISTRALE

PRESENTATA DA:
Francesco Fragnito

RELATORE:
**Chiar.mo Prof.
Gabriele Giovannini**

CORRELATORE:
**Dott.ssa Isabella Prandoni
Dott.ssa Rosita Paladino**

SESSIONE I
ANNO ACCADEMICO 2016/2017

This Thesis work was done as part of the research activity of
the Italian ALMA Regional Centre and of the Istituto di
Radioastronomia - Istituto Nazionale di Astrofisica (INAF) in
Bologna.

*A Nicola e Filomena,
insegnanti di professione e di vita.*

Contents

Abstract	13
1 Introduction	15
1.1 Scientific Background	15
1.1.1 AGN classification and radio galaxies	16
1.1.2 AGN feedback and feeding	20
1.2 The case of NGC 3100	23
1.2.1 The Southern radio galaxy sample	23
1.2.2 NGC 3100 available information	26
2 ALMA	28
2.1 Interferometers: principles and concepts	28
2.1.1 Single-dish response	29
2.1.2 Aperture synthesis	30
2.1.3 Calibration: from observed to real visibilities	33
2.1.4 Imaging process	33
2.2 Observing with ALMA	35
2.2.1 Front End, IF and Local Oscillator	35
2.2.2 Back End and Correlators	36
2.2.3 Water Vapour Radiometer	36
2.2.4 Antennas and performance in Band 6	37
3 NGC 3100: ALMA Observations and Data reduction	39
3.1 Observations	39
3.2 Inspection and data calibration	40
3.2.1 CASA	40
3.2.2 Data import, inspection and flagging	41
3.2.3 A priori calibration	41
3.2.4 Data calibration	43
3.2.5 Data examination	45
3.3 Imaging	47

3.3.1	Continuum image	47
3.3.2	CO line Image	49
4	NGC 3100: Data Analysis	51
4.1	CO line Moment Maps	51
4.2	The CO as molecular gas tracer	53
4.3	Comparison with dust and radio continuum	55
5	Kinematics modelling of the CO disk	59
5.1	Tilted-ring model	59
5.1.1	Fitting algorithms: an overview	63
5.2	NGC 3100 models	65
5.2.1	Model assumptions	65
5.2.2	TiRiFiC models	69
5.2.3	3D-Barolo models	74
5.2.4	Moment 1 maps of the models	87
	Conclusions	90
	Bibliography	92

List of Figures

1.1	Bimodality in the color distribution of local galaxies.	16
1.2	The unification model for AGNs.	18
1.3	Bondi accretion power versus the jet power.	22
1.4	CO(2-1) APEX spectra for eight radio galaxies of the Southern Sample.	25
1.5	Observations of NGC 3100.	27
2.1	Normalized 1-D antenna power response for a 12-m antenna .	29
2.2	Normalized 1-D antenna power response for a 12-m antenna .	31
2.3	uv-plane coverage for NGC3100 observation.	32
2.4	Atmospheric transmission PWV.	35
2.5	Schematic view of ALMA LO and IF system.	36
2.6	Band 6 zenith transmission for PWV.	37
2.7	Typical T_{sys} at zenith for Band 6.	38
3.1	Antennas configuration.	40
3.2	WVR corrections.	42
3.3	T_{sys} table corrections.	43
3.4	Model calibrator.	44
3.5	Solutions for amplitude and phase as a function of time. . . .	45
3.6	Corrected visibilities of J1037-2934 and NGC3100.	45
3.7	Corrected visibilities of J1037-2934.	46
3.8	CO(2-1) double-horned line of NGC 3100.	47
3.9	NGC 3100 continuum image.	48
3.10	NGC3100 continuum image self-calibrated.	49
3.11	NGC3100 CO(2-1) line channel map.	50
4.1	Integrated intensity map (moment 0).	52
4.2	Integrated velocity map (moment 1).	53
4.3	ALMA moment 0 map and continuum.	54
4.4	Moment 0 map over the B-I HST dust image.	56
4.5	ALMA moment 0 map and continuum.	57

4.6	Continuum image of ALMA and VLA.	58
5.1	The bending model.	60
5.2	The orientational parametrization of 3D-Barolo.	61
5.3	TiRiFiC and 3D-Barolo model construction and fitting	64
5.4	Inclination of the model.	67
5.5	Velocity field of a rotating disk with additional non-circular motion.	68
5.6	Moments 1 of NGC 3100 created by Barolo.	68
5.7	TiRiFiC rotational model.	70
5.8	TiRiFiC non-circular model.	71
5.9	TiRiFiC rotational model channel maps.	72
5.10	TiRiFiC non-circular model channel maps.	73
5.11	TiRiFiC models PV diagrams.	74
5.12	3D-Barolo rotational model parameters.	76
5.13	3D-Barolo non-circular model parameters.	77
5.14	Surface brightness produced by Barolo.	77
5.15	3D-Barolo rotational model channel maps.	78
5.16	3D-Barolo local non-circular model channel maps.	79
5.17	3D-Barolo azimuthal non-circular model channel maps.	80
5.18	3D-Barolo local non-circular model channel maps.	81
5.19	3D-Barolo azimuthal rotational model PV diagrams.	83
5.20	3D-Barolo local rotational model PV diagrams.	84
5.21	3D-Barolo azimuthal non-circular model PV diagrams.	85
5.22	3D-Barolo azimuthal non-circular model PV diagrams.	86
5.23	Moments 1 of TiRiFiC models.	87
5.24	Moments 1 of azimuthal 3D-Barolo models.	88
5.25	Moments 1 of local 3D-Barolo models.	88
5.26	TiRiFiC and 3D-Barolo rotation curves	89

List of Tables

1.1	General properties of the Southern Sample radio galaxies. . . .	24
1.2	APEX-1 CO(2-1) line measurements of the Southern Sample. .	26
5.1	List of the Models.	69

Sommario

Questa tesi è parte di un progetto che ha come obiettivo effettuare uno studio completo di differenti componenti galattiche (stelle, gas freddo e caldo) nei nuclei di galassie radio-loud di tipo early-type e ricercare segni cinematici di feeding/feedback che possano essere associati in modo causale alla presenza di getti radio. Per questo scopo è stato selezionato un campione di undici galassie a $z < 0.03$ dalla survey Parkes 2.7-GHz, osservate tramite spettroscopia ottica dal VLT/VIMOS (per la componente stellare e di gas caldo) e dall'interferometro ALMA (per la componente di gas molecolare). In particolare, la tesi è incentrata sulla cinematica del gas molecolare nel centro di una delle sorgenti del campione: NGC 3100, una radiogalassia di tipo FRI ospite di una galassia lenticolare a redshift $z = 0.0088$.

NGC 3100, da osservazioni effettuate dal radiotelescopio APEX a 230 GHz, mostra una riga spettrale del CO(2-1) a doppio corno consistente con la presenza di un disco in rotazione (Laing et al. in prep). La regione più interna di NGC 3100 è stata quindi osservata nella Banda 6 di ALMA durante il Ciclo 3.

Come parte di questa tesi, i dati ALMA sono stati ridotti ed è stato ottenuto un data cube con un beam di 0.73 arcsec^2 dove è chiaramente dettata una riga del CO(2-1) a 230 GHz, che mostra una struttura rotante a forma di anello.

Inoltre, analizzando i dati del continuo di ALMA si possono osservare le regioni più interne dei getti radio della galassia, che sono perfettamente consistenti con le osservazioni effettuate con VLA a 5 GHz e 8.5 GHz con una simile risoluzione spaziale. Un'analisi completa dell'emissione in riga del CO(2-1) è stata effettuata attraverso una mappa d'intensità integrata (*momento 0*) ed una mappa di velocità integrata (*momento 1*). È stata quindi trovata una massa di gas molecolare pari a $M = 1.85 \pm 0.4 \times 10^8 M_\odot$, consistente con ciò che si è trovato con APEX. La mappa del CO è stata quindi confrontata con la distribuzione della polvere (da un'immagine B-I in assorbimento) nelle regioni più interne della galassia ospite. Ciò ha portato ad una soddisfacente sovrapposizione tra le strutture dettate in entrambe

le immagini.

Il disco di gas molecolare mostra una cinematica complessa, con alcuni warp nel campo di velocità.

È stata quindi effettuata una modellizzazione del disco attraverso due software: *TiRiFiC* e *3D-Barolo*. Un confronto tra i risultati dei due programmi è risultato utile per comprendere la cinematica del gas. La modellizzazione ha infatti confermato le assunzioni iniziali circa l'inclinazione ($\sim 60^\circ$) e il position angle ($\sim 230^\circ$) del disco. Ciò ha permesso di produrre e confrontare, infine, campi di velocità puramente rotazionali e campi di velocità con moti non circolari.

Abstract

This thesis is part of a project aimed at providing a comprehensive study of different galaxy components (stars, warm, cold gas) in the core of radio-loud early-type galaxies, and look for kinematical signatures of feeding/feedback loops that can be causally related to the presence of radio jets. For this purpose a complete, volume limited ($z < 0.03$) sample of eleven radio galaxies in the Southern sky was selected from the Parkes 2.7-GHz survey. This sample is the target of VLT/VIMOS integral-field-unit optical spectroscopy (warm gas and stellar components) and ALMA CO line imaging (molecular gas). This thesis inquires into the kinematics of molecular gas in the centre of one of the sources in the sample: NGC 3100, a FRI radio galaxy hosted by a S0 galaxy at redshift $z = 0.0088$.

NGC 3100 was observed with APEX at 230 GHz and showed a CO(2-1) line profile (double-horned) consistent with the presence of a rotating disk (Laing et al. in prep). The inner region of NGC 3100 was then imaged with ALMA at Band 6 during Cycle 3.

As part of this thesis, ALMA data was reduced and a data cube was obtained with a beam of 0.73 arcsec^2 , where a CO(2-1) 230-GHz line was clearly detected. The line is organized in a ring-like rotating structure.

The ALMA radio continuum data, on the other hand, revealed the inner part of the radio jets, entirely consistent with those imaged at similar resolution with the VLA at 5 GHz and 8.5 GHz. A full analysis of the CO(2-1) line emission was made through the integrated intensity map (*moment 0*) and the integrated velocity map (*moment 1*). The mass of the molecular gas resulted in $M = 1.85 \pm 0.4 \times 10^8 M_\odot$, consistent with what found with APEX. The CO map was compared with the distribution of dust (from B-I absorption image) in the inner region of the host galaxy. A nice overlap was found for the structures detected in both images.

The molecular gas disk shows a complex kinematics, with some warps in the velocity field.

Two programs were used to model the disk: *TiRiFiC* and *3D-Barolo*. The comparison of their results was helpful to better understand the kinematics

of the gas. The modelling confirmed initial guesses about the inclination ($\sim 60^\circ$) and the position angle ($\sim 230^\circ$) of the gas disk, and allowed us to derive purely rotational velocity fields as well as fields including non-circular motions.

The thesis is organized in five Chapters:

- In the first Chapter the scientific background is briefly presented as well as the Radio Galaxy NGC 3100.
- In the second Chapter an introduction to radio interferometry and the ALMA telescope is given.
- The third Chapter is focused on the ALMA data reduction of NGC 3100 continuum and CO(2-1) 230-GHz line emission.
- In the fourth Chapter the analysis of the ALMA data is presented, together with a comparison with radio continuum (VLA) and dust absorption images.
- In the fifth Chapter the TiRiFiC and 3D-Barolo modelling programs are presented and their results are discussed.

Chapter 1

Introduction

1.1 Scientific Background

Large-scale properties and scaling relations of early-type galaxies (ETGs) that compare surface brightness, velocity dispersion and stellar mass (e.g. Faber-Jackson, $M - \sigma$ relation) provide important information in order to trace the fossils of galaxy formation processes, as ETGs are old evolved galaxies, that generally present limited star formation and dust content.

The Sloan Digital Sky Survey (SDSS; York et al. 2000) has given a significant contribution in the understanding of formation of local ETGs, based on the statistically significant bimodality in the galaxy colour distribution. Local galaxies can be separated in two distinct groups: the so-called “blue cloud”, mainly constituted by star-forming disk galaxies, and the “red sequence”, constituted by massive and passive ETGs; a minor fraction of galaxies can be found in the so-called “green valley”. This bimodality has been interpreted as the result of galaxy evolution. Galaxies grow with time due to ongoing star formation and move toward the high-mass end of the blue cloud and then rapidly move to the red sequence (Figure 1.1). A mechanism that efficiently suppresses episodes of intense star formation and expels gas from the system is needed in order to allow this rapid transition (e.g. Faber et al. 2007). Several mechanisms have been invoked: active galactic nucleus (AGN) feedback (in the form of quasar winds), supernovae winds, gravitational gas heating or shock heating in massive halos.

On the other hand, dissipationless dry mergers of red sequence galaxies are thought to be responsible for the formation of the most massive ETGs (e.g. Oser et al. 2010), while heating from radio jets (jet-induced feedback) is thought to be responsible for suppressing star-formation in ETGs, and maintaining them on the red sequence (i.e. “red and dead”). Indeed, ETGs

host a wide range of kinematically decoupled components, central stellar disks, and other peculiarities (e.g. Emsellem et al. 2004). The suppression of star formation in ETGs and the formation of sub-structures may well be connected and both related to *AGN feedback* and *fueling* cycles.

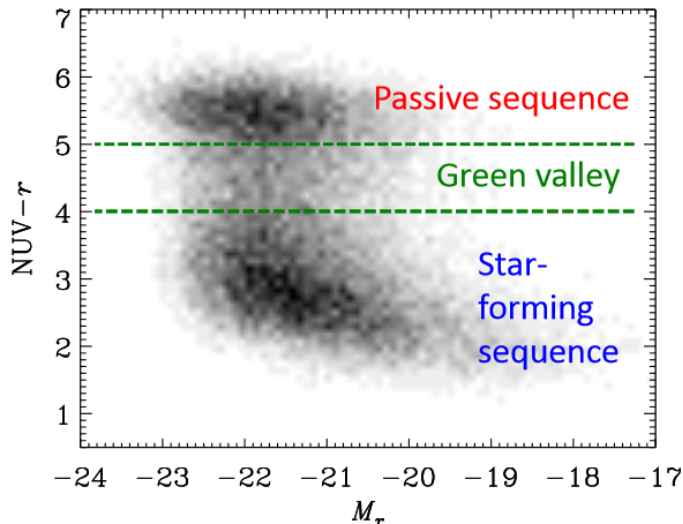


Figure 1.1: UV-optical color magnitude diagram showing the bimodality in the color distribution of local galaxies between star-forming galaxies (blue cloud) and passive galaxies (red sequence) with the transitional green valley. Data from the $z < 0.22$ GALEX/SDSS sample (Salim et al. 2007).

A comprehensive study of the various gas phases, as well as the stellar and dust components in a representative sample of massive, radio-loud ETGs (in which jets are currently active) could provide a crucial comparison to existing studies of radio-quiet ETG samples (e.g. *ATLAS^{3D}*; Cappellari et al. 2011; Young et al. 2011; Alatalo et al. 2013; Davis et al. 2011, 2013a). It will enable a better understanding of the feeding of AGNs, and will isolate the role played by jet-induced feedback (likely dominant in local, massive ETGs) in the overall formation and evolution of ETGs.

Throughout this work distances and luminosity have been computed assuming a CDM cosmology, where: $H_0 = 70 \text{ km s}^{-1} \text{ Mpc}^{-1}$, $\Omega_M = 0.3$ and $\Omega_\lambda = 0.7$.

1.1.1 AGN classification and radio galaxies

The term Active Galactic Nucleus (AGN) generally indicates an extremely energetic phenomenon in the nucleus, or in the central region, of a galaxy.

The basic structure of an AGN is composed by:

- A central *black hole* (BH) with mass ranging from $10^6 M_\odot$ up to $10^{9-10} M_\odot$, probably spinning at some level.
- An *accretion disk* formed by matter attracted by the gravitational potential of the BH.
- A *corona* surrounding the accretion disk and particularly active in emitting X-ray light.
- A region filled by small clouds distant less than one parsec from the BH. This is the so-called *Broad Line Region (BLR)*. It absorbs $\sim 10\%$ of the radiation from the disk and re-emits it in the form of emission lines with typical velocity dispersions of $\sim 3000 \text{ km s}^{-1}$.
- An obscuring *torus* located at several parsec from the BH, that re-processes part of the nuclear radiation and re-emits it in the infrared band.
- A more distant region ($\sim 100 \text{ pc}$) where less densely diffuse clouds are moving with characteristic velocities of $\sim 300 - 500 \text{ km s}^{-1}$ named *Narrow Line Region (NLR)*.

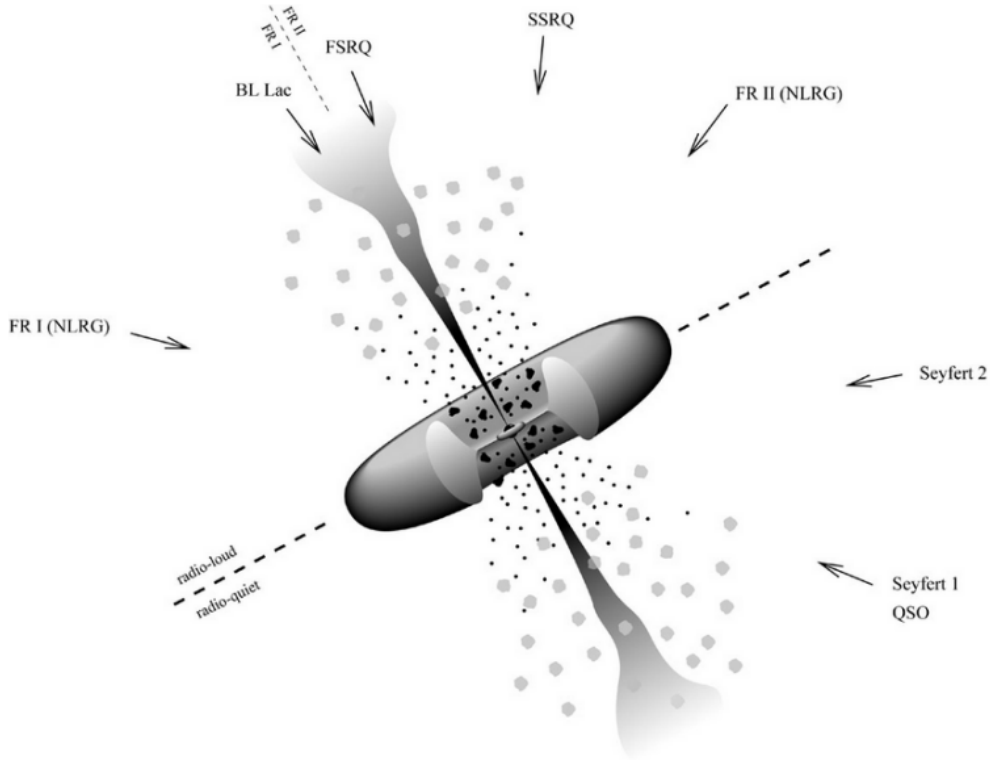


Figure 1.2: The unification model for AGNs. Blazars are RL AGNs for which the jets are close to LoS. They are divided in BL Lacertae objects (BL Lac) and Flat Spectrum Radio Quasar (FSRQ). If the orientation angle is $\sim 30^\circ$ (both NLR and BLR are visible), a RQ quasar (QSO), a Steep Spectrum Radio QSO (SSRQ) or a Seyfert 1 galaxy is observed. At larger angular offsets, the BLR is hidden by the torus, and we observe Narrow Line Radio Galaxies (NLRG) or Seyfert 2 galaxies. Perpendicular to the jet axis, the full extent of the jets (when present) can be seen.

The emission lines coming from the BLR are usually originated by permitted transitions, the most relevant belonging to Balmer and Lyman Hydrogen series. The NLR emits both forbidden and permitted lines, the most evident among the former being the lines produced by ionized Oxygen and Neon.

A basic classification scheme divides AGN in radio-loud (RL) and radio-quiet (RQ) depending on their radio properties. Radio-loud AGNs show two collimated jets of plasma feeding extended lobes or a halo, both emitting in the radio continuum. Radio-quiet AGNs show weak or no large scale jets.

According to the Unification Model (Antonucci, 1993; Urry & Padovani, 1995) the observed AGN properties depend on the inclination of the system with respect to the line of sight (LoS) to the observer. When the observing angle is large, the torus hides the emission from the inner parts of the system

including the BLR. Only the NLR is visible and the object is classified as a Type 2 AGN. When the AGN is viewed at intermediate inclination the inner regions becomes visible together with the NLR, and the AGN is classified as a Type 1 object. RL AGNs whose jets point toward us are called Blazars; when the jets point elsewhere they are called Radio Galaxies (RG). A schematic representation of the classification is shown in Figure 1.2, where different terminology is used depending on whether the AGN is RL or RQ.

Radio Galaxies typically show the following components:

- *Radio Lobes*, extended structures with almost elliptical shape and symmetrical locations with respect to the central object. The distance of the lobes spans from few tens of kpc up to 1 Mpc and their luminosity usually decreases going from the edges to the centre.
- *Hot Spots*, regions with little extension and higher luminosity compared with the lobes. The hot spots usually marks the end point of a well collimated jet for a high power radio galaxy.
- *Core*, central compact component that usually gives little contribution to the overall radio emission. Its contribution is typically larger in low power radio galaxies.
- *Jets*, elongated and narrow structures typically starting from the core. Their end is marked by the hot spots where the material, expelled from the core and funnelled by the jets, hits the surrounding medium. The appearance of the jets depends on their radiative efficiency. A well collimated jet does not show large radiative losses, and virtually all the energy is channelled toward the hot spot, while a radiative efficient jet loses a large amount of its energy on its way and is generally associated to weak or no hot spot.

Fanaroff & Riley (1974) divided the radio galaxies in two classes, known with the names of FRI and FR II, looking at the morphology of the large-scale radio emission. FRI sources appear brighter toward the centre (edge-darkened), while FR II are brighter at the edges (edge-brightened). Furthermore, they noted that the two classes are characterized by different luminosities. Sources with luminosity $L_{radio} \leq 2 \times 10^{25} WHz^{-1} sr^{-1}$ are often (but not always) FRI, while brighter sources are often FR II. The two morphological types clearly show different behaviour in their optical spectra (Laing et al. 1994, Buttiglione et al. 2010). The FRI radio galaxies hosts typically exhibit optical spectra with absorption lines and/or low ratios of $O[III]/H_{\alpha} < 0.2$

. Following the classification of Laing et al. (1994) these galaxies are classified as Low Ionization Emission Line Radio Galaxies (LERGs). On the other hand, FRII host galaxies appear as a mixed class: they can show either FRI-like spectra or strong high ionization emission lines characterized by $O[III]/H_\alpha > 0.2$ (High Ionization Emission line Radio Galaxies, HERGs).

Observational evidence is growing that LERGs constitute a different type of AGNs that does not fit into the unification model and a distinct mode of accretion onto the supermassive black hole (SMBH) exists (advection-dominated, ADAFs, or radiatively inefficient accretion flows, RIAFs). These types of AGN are often capable of launching two-sided jets and lack a dust torus. The geometrically-thin accretion disk is either absent, or is truncated in the inner regions and it is replaced by a geometrically-thick structure in which the inflow time is much shorter than the radiative cooling time (Heckman & Best, 2014).

1.1.2 AGN feedback and feeding

SMBHs are thought to play a principal role in regulating star formation in galaxies across cosmic time. The process by which this occurs is known as AGN feedback and it takes place through an interaction between the energy and radiation released by black hole accretion and the gas in the host galaxy.

Two major modes are identified, differentiated by the nature of the energy outflow near the black hole. The first is the so-called *radiative mode*. This feedback takes the form of quasar-driven winds that expel gas from the galaxy centre. It is typically associated with black hole accreting close to the Eddington limit. The second mode is the so-called kinetic mode, also known as *jet mode*. In this case the energy is released in form of collimated jets that wipe out the intra-galactic medium on their way and heat the surrounding gas. It tends to occur in massive galaxies embedded in hot gas halos (Fabian 2012). In particular, radio-emitting jets are common in massive elliptical galaxies at the centre of galaxy clusters and lead to the formation of cavities in the intergalactic medium (IGM) surrounding them. The radio jets are thought to heat the gas in the so-called cool-core clusters, preventing further cooling and thereby suppressing star formation. This should also prevent further fueling of the BH and eventually lead to the switch off of the radio jets. However, many details are missing and the mechanisms by which jetted AGN are fuelled and the way in which this forms part of a feedback loop are not yet fully understood.

Two principal accretion modes are invoked for the AGN feeding: the *cold accretion* (accretion of cold circumnuclear gas) or accretion from hot keV

atmosphere (*Bondi accretion*). We have seen that RGs can be divided in the two classes of HERGs and LERGs. These two classes are characterized by different accretion rate onto the central SMBH. The first class, *radiative mode AGN*, accrete at $\geq 1\%$ of the Eddington limit. In the second class, *jet mode AGN*, the accretion rate and the radiative output from the AGN are both much lower (Heckman & Best, 2014).

Allen et al. (2006) have found that the rate of accretion of the X-ray emitting gas at the accretion radius (the radius within which the gravitational potential of the central black hole dominates over the thermal energy of the surrounding X-ray emitting gas) can be written as (Bondi, 1952):

$$\dot{M}_{Bondi} = 4\pi\lambda(GM_{BH})^2c_s\rho$$

where ρ is the density of the gas at the accretion radius, M_{BH} is the central black hole mass, G is the gravitational constant, c_s is the adiabatic sound speed of the gas at the accretion radius and λ is a numerical coefficient that depends upon the adiabatic index of the accreting gas. For an efficiency η , the maximum power released from the black hole system is

$$P_{Bondi} = \eta\dot{M}_{Bondi}c^2.$$

They found a correlation between the Bondi accretion rate and jet power for LERGs and proposed that accretion in these systems may occur directly from the hot phase of the IGM (Figure 1.3). Indeed, the kinetic power of the jets was computed through the estimates of the energy E required to create observed cavities in the X-ray emitting gas by the jets and the life time of these cavities t_{age} :

$$P_{jet} = \frac{E}{t_{age}}.$$

Subsequently, Hardcastle et al. (2007) confirmed that the energy required to power non-thermal emission from LERGs could be provided by Bondi accretion. This is not the case for HERGs where an extra component is needed to sustain the observed jet powers. The most plausible candidate for this extra-component is cold gas brought to the center through mergers (*cold accretion*).

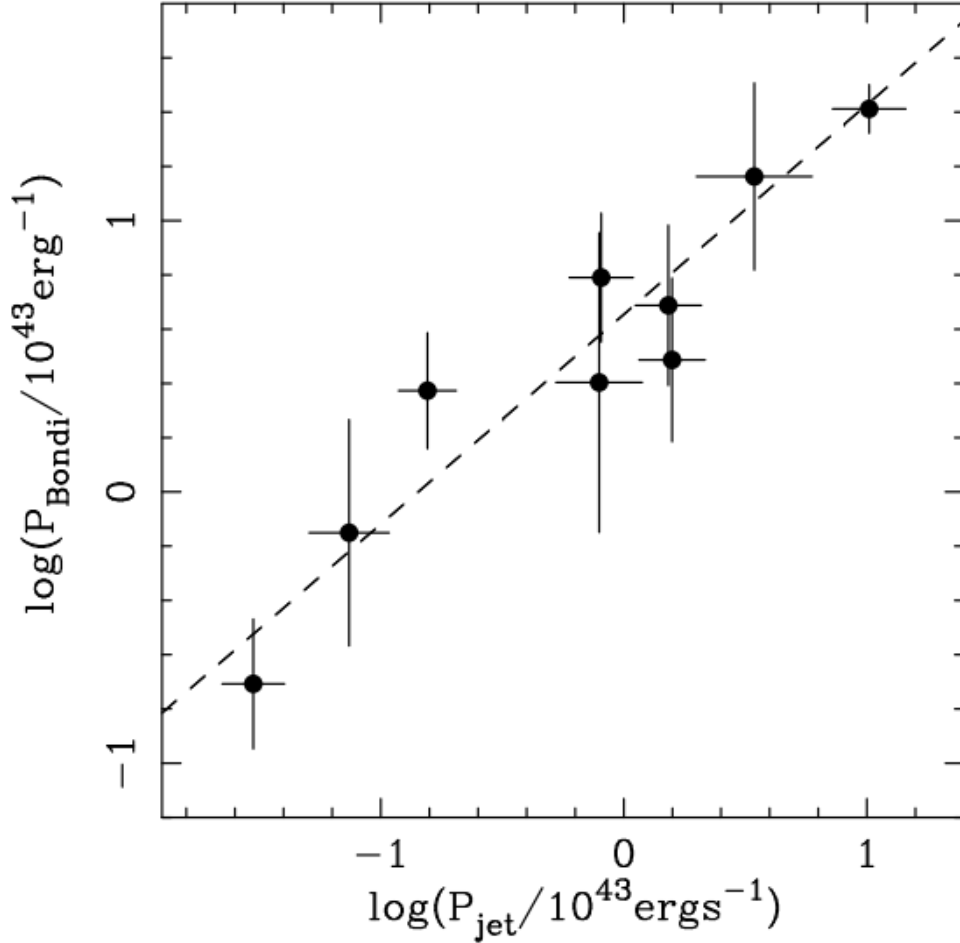


Figure 1.3: The logarithm of the Bondi accretion power versus the logarithm of the jet power. Both the quantities are in units of $10^{43} \text{ erg s}^{-1}$. The dashed lines shows the bestfitting linear-plus-constant model.

Even though enough energy can be provided by accretion of hot gas at the Bondi rate, this does not prove that LERGs are powered in this way. The reason is that the mass of material actually reaching the black hole may be significantly lower than the Bondi estimate, as spherical symmetry must break down at some radius.

Russel et al. (2013) re-examined the relationship between the jet power and the Bondi accretion rate. The results indicate weaker evidence for a correlation between Bondi accretion and jet power. He suggested that cold gas fuelling could be a likely source of accretion power in these objects, even if he could not rule out Bondi accretion, which could play a significant role in low-power jets.

This gas may cool from the hot phase, as in the ‘cold feedback’ or ‘chaotic cold accretion’ models (Pizzolato & Soker, 2005; Gaspari et al., 2013), but could also come from stellar mass loss, interactions or mergers. Some support for the idea that at least the most powerful LERGs are fuelled by accretion of cold gas comes from the direct detection of dust and cold molecular gas in these systems (de Ruiter et al., 2002; Lim et al., 2003; Leon et al., 2003; Prandoni et al., 2007, 2010; Ocaña Flaquer et al., 2010). But the presence of large masses of molecular gas is not direct evidence of fuelling. Dust in radio galaxies is often localised in well-defined disks on small scales ($\leq 2.5 \text{ kpc}$). Similarly, the observed CO line profiles often show the double-horned profiles characteristic of rotating disks. Very few high-resolution images of CO emission are available, but Okuda et al. (2005) made interferometric observations of the radio galaxy 3C 31 and showed that the CO, which coincides spatially with the dust disk observed in HST images, is in ordered rotation. If the cold gas is in stable orbits, as suggested by Okuda et al. (2005), then the accretion rate may be relatively low. In other galaxies, the molecular gas appears to be outflowing (or more generally interacting with) the radio jets or lobes. The incidence of these different types of molecular gas distribution in typical radio galaxies (as opposed to extreme cases) is not known. The key instrument for such an analysis is ALMA. However, very little is currently known about cold gas in the southern radio galaxies that can be observed at high elevation with ALMA. For this reason a complete volume-limited sample of radio galaxies in the Southern hemisphere has been selected for systematic CO observations.

1.2 The case of NGC 3100

1.2.1 The Southern radio galaxy sample

The Southern radio galaxies sample was selected from the Parkes 2.7-GHz survey. This survey collects 191 RGs located in the declination range $-17^\circ < \delta \leq 40^\circ$ with a radio flux-density limit of 0.25 Jy at 2.7 GHz and an optical magnitude limit of $m_V \leq 17.0$ (Ekers et al. 1989). The two selection criteria applied to select the Southern radio galaxies sample were:

- association of the source with an Elliptical or S0 galaxy
- host galaxy redshift $z < 0.03$

The eleven selected sources have all low or intermediate radio powers and a FRI radio morphology.

Radio source	Host galaxy	z	$S_{1.4\text{GHz}}$ mJy	$\text{Log } P_{1.4\text{GHz}}$ (W Hz ⁻¹)	FR type	m_K mag	M_K mag	σ km s ⁻¹	dust	T_{dust} Kelvin	M_{dust} M_{\odot}
PKS 0007-325	IC 1531	0.025641	582	23.9	FRI	9.554	-25.70	222.6	—	—	—
PKS 0131-31	NGC 612	0.029771	4980	25.0	FRI/II	9.575	-26.01	—	dust lane ^d	38.8	7.2
PKS 0320-37	NGC 1316	0.005871	314	22.4	FRI	5.587	-26.44	225.9	dust patches ^b	38.4	6.0
PKS 0336-35	NGC 1399	0.004753	632	22.5	FRI	6.306	-25.25	341.9	no dust ^b	<24.4	<5.3
PKS 0718-34	—	0.028353	2050	24.6	FRI	9.969	-25.59	—	dust patches ^c	—	—
PKS 0958-314	NGC 3100	0.008813	541	23.0	FRI	8.077	-24.85	199.9	dust lane ^d	33.3	5.7
PKS 1107-372	NGC 3557	0.010300	777	23.3	FRI	7.203	-26.08	269.5	face-on disk ^b	35.9	5.6
PKS 1258-321	ESO 443-G 024	0.017042	1465	24.0	FRI	8.507	-25.87	274.7	no dust ^c	37.1	<5.1
PKS 1333-33	IC 4296	0.012465	64282	25.4	FRI	7.502	-26.18	333.2	edge-on disk ^b	49.7	4.8
PKS 2128-388	NGC 7075	0.018479	963	23.9	FRI	9.562	-24.98	259.9	—	22.7	7.4
PKS 2254-367	IC 1459	0.006011	1273	23.0	FRI	6.805	-25.27	306.1	dust lane ^b	40.9	5.1

Table 1.1: General properties of the Southern Sample radio galaxies. From col. 1 to col. 3: radio source name, host galaxy name and redshift. In col. 4 and 5: the radio flux density at 1.4GHz and corresponding radio power. In col. 6, the FR type. In col. 7 and 8: the apparent and absolute magnitudes in K band. Then, in order of columns: velocity dispersion, optical dust morphology, dust temperature and mass from IRAS observations. The optical dust information come from: (a) Bettoni et al. (2001); (b) Lauer et al.(2005); (c) Colbert et al. (2001); (d) Sandage & Brucato (1979), (e) Govoni et al. (2000).

The main characteristics of the Southern Sample galaxies are listed in Table 1.1. Emission in the CO(2-1) transition at 230 GHz rest frequency was investigated for ten of the eleven sources with the APEX single dish telescope (Prandoni et al. 2010; Laing et al. in prep). The 27 arcsec APEX Half Power Beam Width probes the presence of molecular gas in the inner 2.7-16.2 kpc of the host galaxies (depending on redshift). This allows a direct comparison with the dust structures on similar scales imaged with HST, when available (Lauer et al. 2005). All sources were detected at either 40 or 80 km^{-1} velocity resolution. In Figure 1.4 are shown eight CO(2-1) APEX spectra (of the ten obtained) discussed in Laing et al. (in prep.).

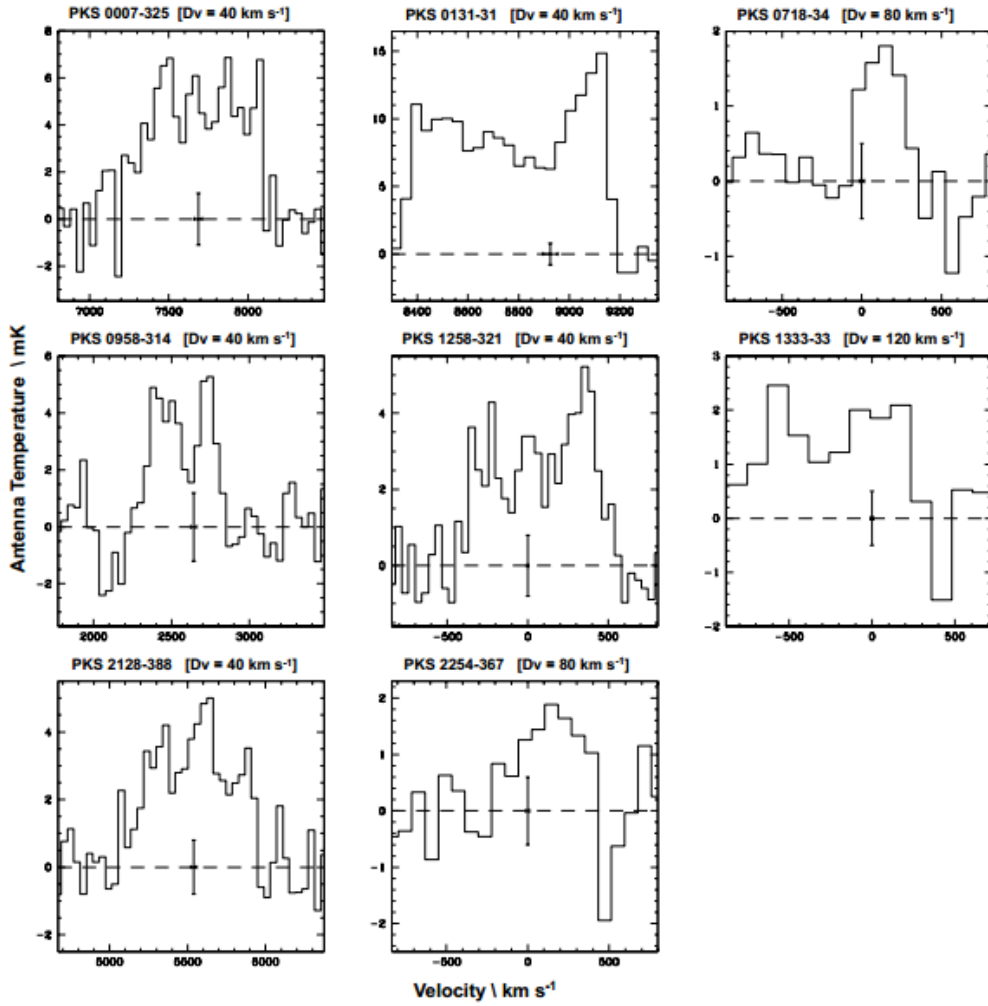


Figure 1.4: CO(2-1) APEX spectra for eight radio galaxies of the Southern Sample. Dv is the velocity channel width. The vertical and horizontal error bars at the systemic velocity (V_{sys}) indicate the RMS on the Antenna Temperature and the error on V_{sys} , respectively. From Laing et al. (in prep.).

Source	t_{ON} min	T_{sys} K	Δv_{res} km s ⁻¹	T_a^{rms} mK	T_{peak} mK	S/N	Δv_{FWHM} km s ⁻¹	$\Sigma T_a dv$ K km s ⁻¹	M_{H_2} $10^7 M_\odot$	R kpc
PKS 0007-325	34	192	40	1.1	6.9	6.3	771	3.83	18.8±6.7	13.9
PKS 0131-31	64	190	40	0.8	15.0	18.8	774	7.19	284.9±32.9	16.2
PKS 0718-34	83	214	80	0.5	1.8	3.6	334	0.50	18.0±5.0	15.4
PKS 0958-314	62	191	40	1.2	5.3	4.4	446	1.68	6.1±1.1	4.9
PKS 1258-321	106	195	40	0.8	4.6	6.0	786	2.39	31.4±0.4	9.3
PKS 1333-33	55	207	120	0.5	2.5	5.0	864	1.50	10.0±0.2	6.9
PKS 2128-388	52	199	40	0.8	5.0	6.3	650	2.18	36.6±4.8	10.1
PKS 2254-367	79	227	80	0.6	1.9	3.2	492	0.70	0.8±0.3	3.4
PKS 0336-35 ^a	108	272	120	0.4	1.3	3.5	365	0.39	2.0±0.9	2.7
PKS 1107-372 ^a	18	316	40	2.0	7.0	3.5	248	1.52	31.6±6.7	5.6
PKS 0320-37 ^b	—	—	—	—	—	—	500	—	~35.0	3.9

Table 1.2: APEX-1 CO(2-1) line measurements of the Southern Sample. (a) Sources studied by Prandoni et al. (2010), (b) Source studied by Horellou et al (2001)

For the majority of the sources the CO lines show double horn or flat profiles, consistent with ordered rotation. The Southern Sample RGs typically show large linewidths ($\geq 500 \text{ km s}^{-1}$), and the derived molecular masses span a range between $10^{7-9} M_\odot$ (see Table 1.2).

1.2.2 NGC 3100 available information

Nine of these radio galaxies were followed up with ALMA during cycle 3. In this thesis I present the ALMA data analysis for one of them: NGC 3100 ($RA(J2000) = 10 : 00 : 40.8$; $DEC(J2000) = -31 : 39 : 52$).

NGC 3100 is FRI radio galaxy (left panel of Figure 1.5) hosted by a S0 galaxy at redshift $z = 0.0088$ corresponding to a luminosity distance $D_L = 40.9 \text{ Mpc}$.

Figure 1.4 shows that NGC 3100 (PKS 0958-314) is characterized by a double-horn CO profile on a scale of (at least) $\sim 5 \text{ kpc}$ (see Table 1.2), consistent with the presence of a rotating disk. In addition NGC 3100 shows a patchy dust morphology (right panel of Figure 1.5).

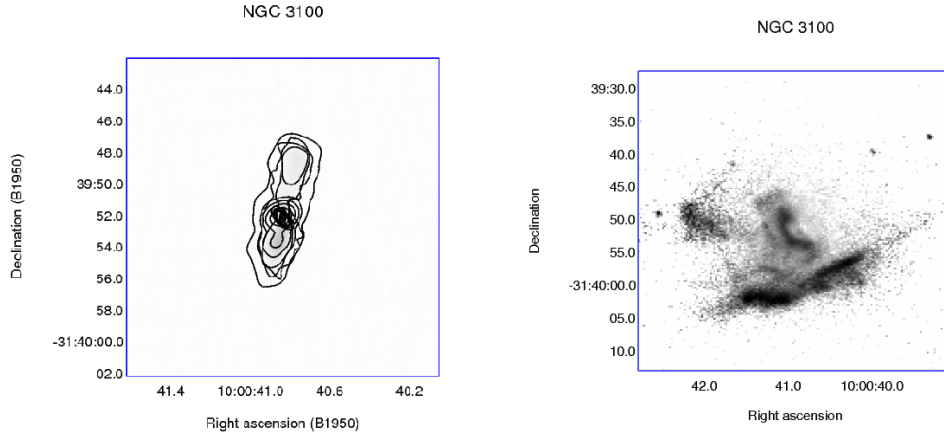


Figure 1.5: Observations of NGC 3100. Left : 5 and 8.5 GHz VLA radio continuum image showing a twin radio jet. Right: NGC 3100 optical B-I image showing the central diffuse dust.

NGC 3100 can be spectroscopically classified by using the standard $[OIII]\lambda 5007/H\beta$ versus $[NII]\lambda 6583/H\alpha$ BPT diagnostic diagram (Baldwin, Phillips and Terlevich 1981) and its following revisions (Kewley et al. 2001, Kauffmann et al. 2003, Kewley et al. 2006). In such a diagram galaxies which are likely to be dominated by an AGN can be separated from galaxies dominated by star formation. In addition Seyfert galaxies can be distinguished from Low Ionization Nuclear Emission Regions (LINER) galaxies. In this manner, Dopita et al. (2015) identifies NGC 3100 as a LINER with very low extinction, but with deep NaD absorption. As such, NGC 3100 belongs to the LERG class.

Chapter 2

ALMA

The Atacama Large Millimeter/submillimeter Array (ALMA) is an aperture synthesis array operating in the millimeter and submillimeter regime. It is located on the Chajnantor plain of the Chilean Andes, 5000 m above sea level, where the site offers the best weather conditions required to observe in (sub)mm wave range.

In September 2011, the telescope started its Early Science period with a reduced number of antennas, frequency bands, array configurations and observing modes. ALMA consists of two principal arrays:

- *12-m Array*, composed by fifty 12-meter antennas, that can be arranged in different configurations with baselines from 15 m up to 16 km.
- *Atacama Compact Array (ACA)*, composed by twelve 7-m antennas (with 9 to 30 m baselines) plus four 12-m single-dishes, designed to solve the so-called *zero-spacing problem* (See Section 2.1.2).

The ALMA observations used for this thesis have been taken during Cycle 3, with the *12-m array*. The basics of Interferometry and the main characteristics of ALMA will be illustrated in this Chapter.

2.1 Interferometers: principles and concepts

Interferometry is an observational technique used in millimeter/radio and visual regime, based on the principle of interference of incoming electromagnetic waves. It involves coherent arrangement of sky signals received by separated antennas pointed to the same object. The signals are interfered, allowing the sampling of sky brightness distribution on an angular scale smaller than what is possible with the single antennas composing the array.

2.1.1 Single-dish response

According to the Fraunhofer diffraction theory, it is possible to consider the electromagnetic (EM) power of wavelength λ from a point-like source at infinity arriving at an antenna of diameter D essentially as plane-parallel wavefronts along its axis. The diffraction pattern in the aperture of an antenna is related to the power distribution through a Fourier transform. This results into the so-called power pattern, or *beam*. It represents the response in the focal plane of the antenna to EM signal (Figure 2.1).

The on-axis central Gaussian-like feature is called *primary beam* or *main-lobe* and it has a Half Power Beam Width (HPBW) of $\sim \lambda/D$, where λ is the wavelength of the incident wave and D is the diameter of the antenna. *Sidelobes* at off-axis angles may be identified. They are related to summed EM interference, decreasing with increasing angular off-set. The distance between nulls is defined Beam Width at First Nulls (BWFN) with a value of $2.44\lambda/D$. Half the BWFN of the primary beam, $1.22\lambda/D$, is the Rayleigh resolution of the antenna, the minimum angular distance between two objects for which they can be seen as separated. The beam is affected by various effects that may corrupt the measured power, such as surface imperfections or diffraction from other antenna components.

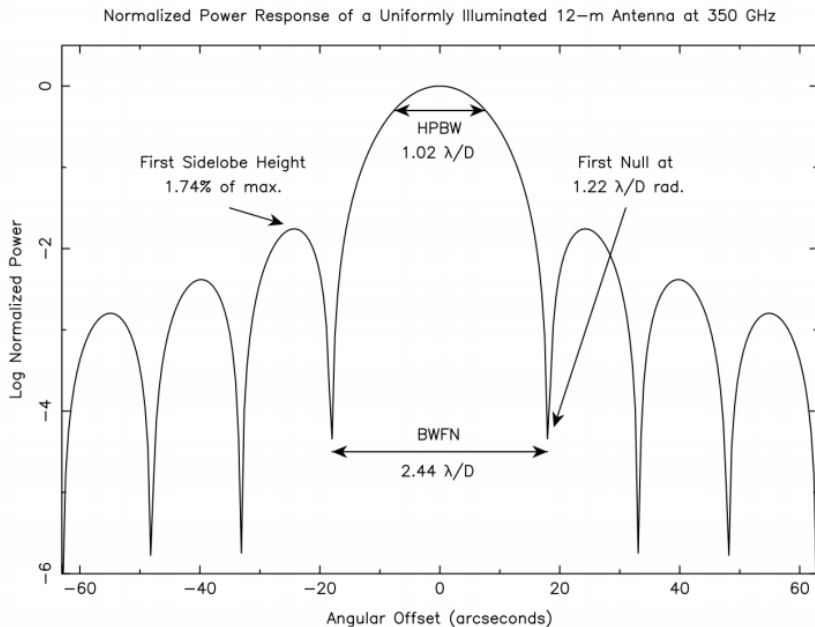


Figure 2.1: Normalized 1-D antenna power response for a 12-m antenna uniformly illuminated at 300 GHz. The power is in log units to emphasize the sidelobes. HPBW measured from actual 12-m ALMA antennas is $\sim 1.13\lambda/D$.

The actual ALMA antennas were constructed to provide the best response with a nearly gaussian primary beam and low sidelobes with HPBW values of $\sim 1.13\lambda/D$ for the 12-m antennas. This value is the so-called *Field of View (FoV)*:

$$FoV \sim 1.13\lambda/D \quad [radians]$$

The total power received by each antenna is defined as:

$$P_{rec} = \frac{1}{2} A_e \int_{4\pi} I_v(\theta, \phi) P_N(\theta, \phi) d\Omega$$

where A_e is the effective area of the antenna, θ and ϕ are the sky coordinates, $I_v(\theta, \phi)$ the directional function of the sky brightness distribution and $P_N(\theta, \phi)$ the normalized antenna power pattern. The value 1/2 is due to the fact that the receiver is generally sensitive to only one mode of polarization.

The effective area of antennas differs from their geometric area ($\pi(D/2)^2$) by a factor

$$\eta_A = \frac{A_e}{A_{geom}} \leq 1$$

2.1.2 Aperture synthesis

As shown, the resolution of a single-dish observation increases with λ , and decreases with the diameter D of the antenna. In particular, radio/(sub)mm observations have typically poor resolution, as the value of λ is much larger (compared to optical observations) while the maximum antenna diameter D is limited by technique.

For this reason, interferometry, or aperture synthesis, is used to improve angular resolution of the system. An interferometer is composed by two or more antennas, whose signals are combined.

Each pair of elements is spaced by a distance b called baseline (Figure 2.2). The power response of the antennas of a pair is time-averaged and cross-correlated by the correlator. The multiplication of the voltage patterns from element pairs is the resulting power pattern of the interferometer.

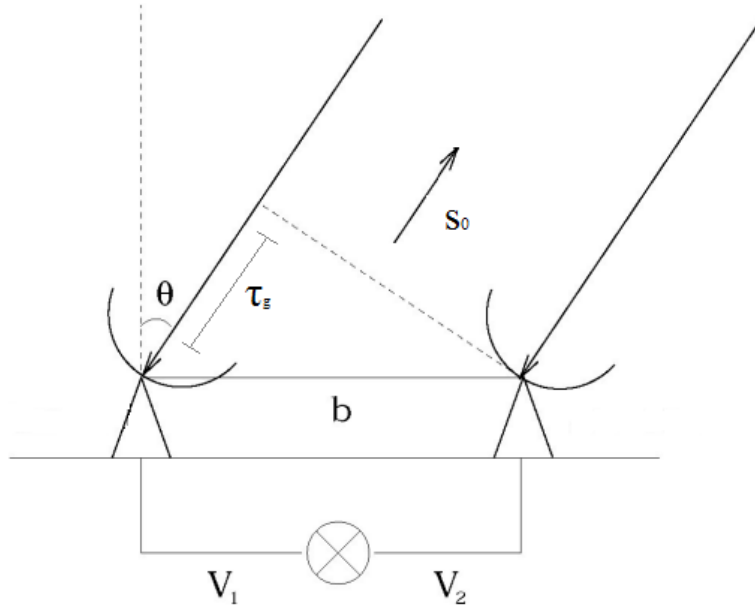


Figure 2.2: Interferometer consisting of two antennas, spaced by a physical distance b . The antennas are both pointed towards a sky location s_0 , distant θ from the meridian.

As two antennas observe the same object with a delay given by $\tau = bs_0/c$, where s_0 is the position observed by the antennas and c is the light-speed, it is applied an artificial delay to the signal received by the first antenna before correlating the signals. At this point, the correlator multiplies and time-averages the signals coming from the two receivers and measures the so-called quantity *complex visibility*, $V(x, y)$.

The complex visibility is the Fourier transform of the sky brightness distribution $B(x, y)$ (*Cittert-Zernike theorem*):

$$V(u, v) = \iint B(x, y) e^{2\pi i(ux+vy)} dx dy = V_0 e^{i\phi}$$

$$B(x, y) = \iint V(u, v) e^{-2\pi i(ux+vy)} du dv$$

where u and v components (in λ units) are the projection of each baseline onto the observed sky-plane in E-W and N-S directions, the x and y spatial components (in radians) are the position in the sky plane. The visibility V gives information about source brightness and phase centre through its amplitude V_0 and its phase ϕ .

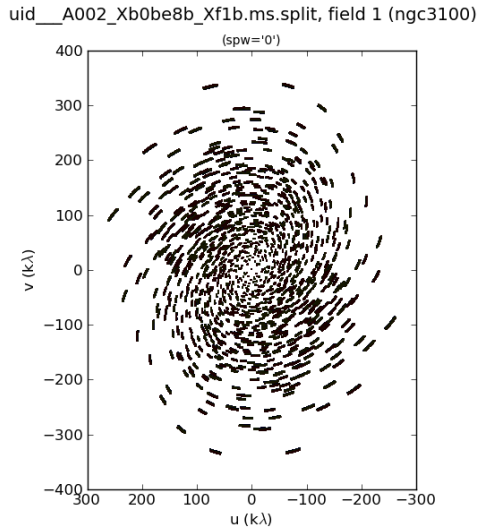


Figure 2.3: uv-plane coverage for the NGC3100 Cycle 3 ALMA observation. The integration time is 44min; u and v are in meter unit.

The *uv-plane* as visibility distribution gives information about sky brightness distribution on the sampled angular scales.

The sky sampling carried out from a pair results in a brightness distribution on a scale inversely proportional to its length ($\sim \lambda/b$ for the 1-D case). The short baselines sample larger scale and the longer ones sample shorter scale. Observing shorter or longer wavelengths sample smaller or larger angular scales, respectively. Different antennas pairs allow to sample different scales, corresponding to different points in the uv-plane (Figure 2.3). The baselines projection plane is affected by the Earth's rotation that changes the position of the uv points, allowing to sample more scales.

Interferometer properties

As seen for the single-dish, the *FoV* in aperture synthesis represents the angular sensitivity pattern on the sky of each element in the array. In this case it is also named **primary beam** keeping the same physical definition

$$FoV \sim 1.13\lambda/D \quad [radians]$$

The angular resolution of an interferometer, called **synthesized beam**, can be written as:

$$\theta_{res} = k \frac{\lambda}{B_{max}} \quad [radians]$$

where k is related to visibilities weighting and B_{max} is the longest baseline in the array.

Baselines shorter than the diameter of an antenna are impossible to be produced. This introduces the so-called *zero-spacing problem*: regions of the uv -plane related to distances closer than the minimum baseline cannot be sampled. For this reason, there is a maximum angular scale structure that an interferometer recovers, the Maximum Recoverable Scale (**MRS**):

$$\theta_{MRS} \approx 0.6 \frac{\lambda}{B_{min}} \quad [radians]$$

where B_{min} is the minimum baseline of the array configuration.

2.1.3 Calibration: from observed to real visibilities

Instrumental and atmospheric effects corrupt the visibilities obtained with an interferometer. For this reason, calibration is needed to correct such effects and to recover the real visibilities from the observed ones.

The Hamaker-Bregman-Sault *Measurement equation* expresses the relationship between observed and real visibilities for a baseline between antenna i and j :

$$V_{ij}^{obs}(\nu, t) = G_{ij} V_{ij}^{real}(\nu, t) + noise$$

where V_{ij}^{obs} represents the observed visibilities, V_{ij}^{real} represents the corresponding real ones and G_{ij} are the gain factors and represent the combination of all the corruption factors related to the baseline ij .

The gain factors can be decomposed into time-dependent and frequency-dependent components, which are assumed to be independent from each other:

$$G = B(\nu)J(t)$$

where $B(\nu)$ represents the frequency-dependent components and $J(t)$ represents the time-dependent components.

The measurement equation is solved by observing one or more calibrator sources with known properties to determine the different gain factor. Once solutions are found, the gain factors are stored in calibration tables and applied to the observed visibilities of the science target (See Section 3.2.4).

2.1.4 Imaging process

The observed visibilities of a target are ideal visibilities sampled only in discrete points of the uv -plane. This can be expressed as:

$$V(u, v)_{meas} = S(u, v) \cdot V(u, v)_{true} \quad (1)$$

where $V(u, v)_{meas}$ are the observed visibilities, $V(u, v)_{true}$ are the ideal visibilities and $S(u, v)$ is the so-called sampling function, an 1-result indicator function ($S(u, v) = 1$ where data are taken, $S(u, v) = 0$ where no data are available).

The measured sky brightness distribution is obtained by computing the inverse Fourier transform of (1), achieving the so-called *dirty image*:

$$I_{meas} = FT^{-1}(V_{meas}) = FT^{-1}(S) \otimes FT^{-1}(V_{true})$$

where I_{meas} is the measured sky brightness distribution, and the inverse Fourier transform of the sampling function is called *dirty beam*.

The incomplete spatial frequency sampling produces aliased features in the resulting image. The CLEAN algorithm is an iterative method which makes a deconvolution of the dirty image from the dirty beam to minimize these effects. It proceeds as follows (considering *Hogbom algorithm*):

- Initializes the residual map to the dirty map, and the Clean component list to an empty value;
- Identifies the pixel with the peak of intensity (I_{max}) in the residual map, and adds to the clean component list a fraction of $I_{max} = \gamma I_{max}$, ($\gamma \sim 0.1, 0.3$);
- Multiplies the clean component by the dirty beam and subtract it to the residual map;
- Iterates until stopping criteria are reached: $|I_{max}| <$ multiple of the rms (when rms limited); $|I_{max}| <$ fraction of the brightest source flux (when dynamic range limited);
- Multiplies the clean components by the clean beam, which is an elliptical Gaussian fitting of the central region of the dirty beam, and add it back to the residual (restore).

During the imaging process it is possible to modify the weight of the visibilities considering the *weighting function* $W(u, v)$. It permit to change image resolution and sensitivity. The true density distribution of the visibilities in the *uv-plane* is given by *natural weighting* ($W(u, v) = 1/\sigma^2(u, v)$, where σ is the noise variance of the visibilities) that maximizes sensitivity and produces a larger synthesized beam. *Uniform weighting* gives higher resolution and lower sensitivity by removing the dependencies of spatial-scale sensitivity on the density of sampled visibilities ($W(u, v) = 1/\delta_s^2(u, v)$, where δ is the density of visibilities in a uniform region of the *uv-plane*). *Briggs weighting* is a compromise between the two. It uses the *robust* parameter that varies from natural to uniform.

2.2 Observing with ALMA

Signals are processed by ALMA antenna instruments through specific steps.

After the parabolic dish has collected the signal, this is reflected to the focal plane to be down-converted at the Front End, where the cooled receivers are located. Then, the Back End digitizes the analog signals and sends them to the Correlator, which correlates the signals from each antenna pair. Finally, signal and weather data are sent to the Operation Support Facility, located at 2900 m, where they are quality-checked and archived.

2.2.1 Front End, IF and Local Oscillator

The receivers are located in the secondary focus of the Cassegrain antennas, always kept at a temperature of $20^{\circ}C$. The ALMA front end can accommodate up to 10 receiver bands, which cover wavelengths from 10 to 0.3 mm (30-950 GHz) and located in correspondence to atmospheric transmission windows (Figure 2.4). In Cycle 3, Band 3, 4, 6, 7, 8, 9, and 10 were available.

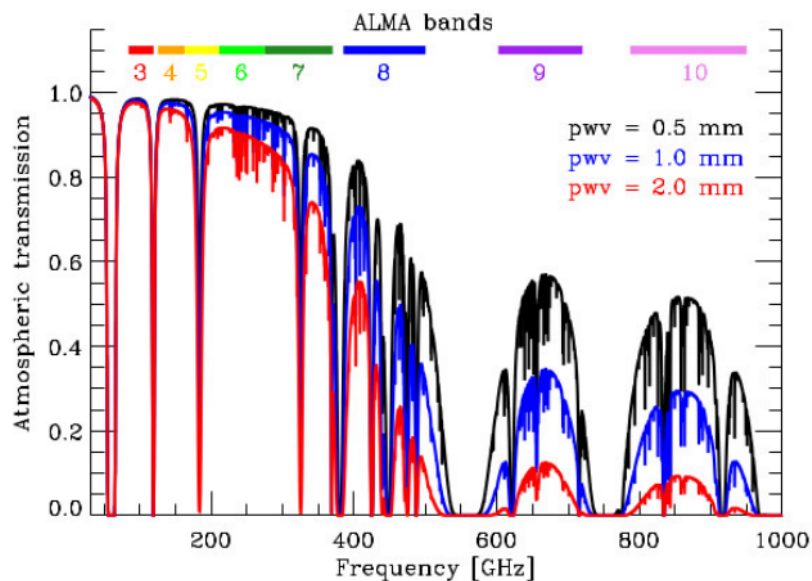


Figure 2.4: Atmospheric transmission curves at Chajnantor Plateau (ALMA site) for different amounts of precipitable water vapour. The horizontal colored bars represent the frequency ranges of the ALMA bands.

The ALMA front end consists of a large cryostat, which is kept at $T = 4K$. It contains the mixer, IF (Intermediate Frequency) and LO (Local Oscillator)

electronics of each band. The receiving systems are sensitive to orthogonal linear polarization.

The IF and LO systems down-convert the sky frequencies to frequency bands of 0-2 GHz each. This work is realized in different stages. The first one splits the signal in the so-called upper sideband (USB) and lower sideband (LSB) in order to down-convert it to 4/8 GHz IF bands. The second down-conversion creates 2 GHz Basebands (BBs) that are allocated in USB and/or LSB. The spectral signal is divided into different spectral windows (SPWs), obtaining bandwidths up to 1.85 GHz. Then, the correlator operating mode will choose the number of channels in which the SPWs will be divided again, depending on the requested spectral resolution (Figure 2.5).

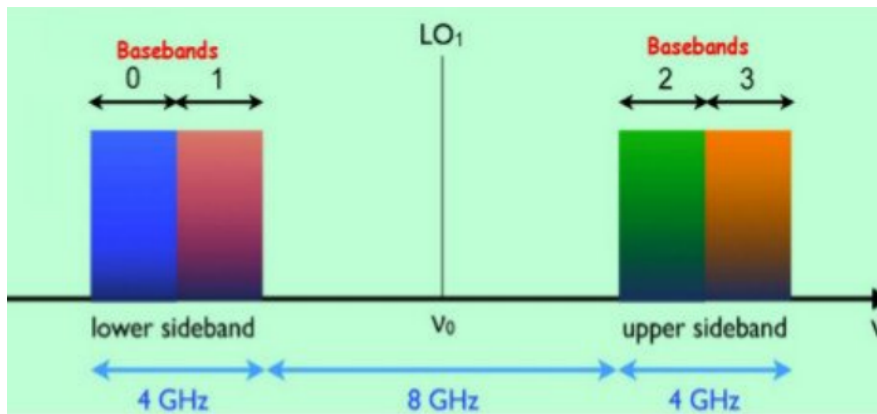


Figure 2.5: Schematic view of ALMA LO and IF system.

2.2.2 Back End and Correlators

The observed signals are down-converted, sampled, quantized in digitizers and then transferred to the correlator, which calculates cross-correlations and auto-correlations for each antenna pair and produces complex visibilities.

Correlators have two work modes: Time Division Mode (TDM) and Frequency Division Mode (FDM). The first one, TDM, provides wide bandwidth and low spectral resolution in continuum observations, while FDM allows a high spectral resolution. For this reason, for spectral-line observations the FDM is preferred .

2.2.3 Water Vapour Radiometer

The *water vapour radiometer* (WVR) observes the variations in the water vapour distribution in the troposphere that affect the observations. Phase

fluctuations (phase noise), which degrade the measurements at millimetric and submillimetric wavebands, are the effect of this variations. The WVR measures and estimates the amount of precipitable water vapour (PWV) along a given LoS to give the right phase corrections for each baseline. WVR measurements are taken on 1-second timescale to carefully sample the actual variations in the atmosphere. WVR is implemented on each 12-m antenna, but not on 7-m antennas (the compactness of the ACA baselines makes phase noise negligible).

2.2.4 Antennas and performance in Band 6

The observations analyzed this thesis were taken in Band 6. In the following we give an overview of the system and instrumentation in this Band.

Band 6 covers the frequency range 211-275 GHz. It possesses dual side-band receivers, with the two sidebands available simultaneously, an IF frequency range of 5-10 GHz and a bandwidth of 7.5 GHz. This Band is affected by several narrow atmospheric absorption lines, most of which are from O_3 (Figure 2.6).

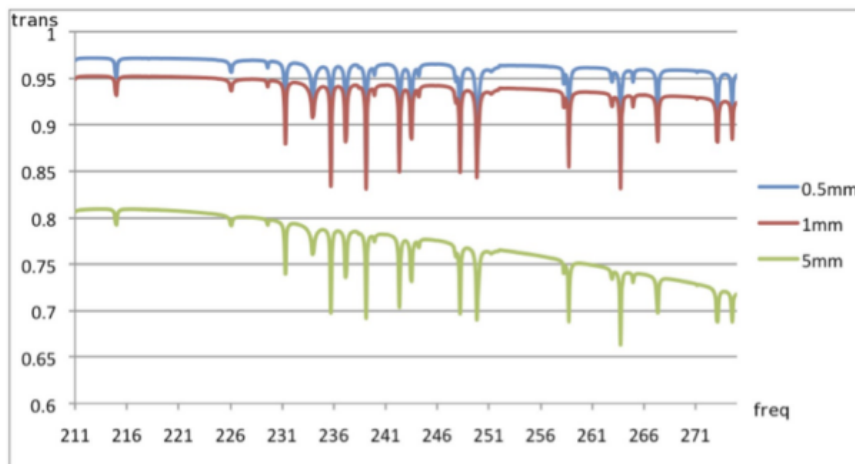


Figure 2.6: Band 6 zenith transmission for PWV=0.5, 1 and 5 mm. Frequency is in GHz.

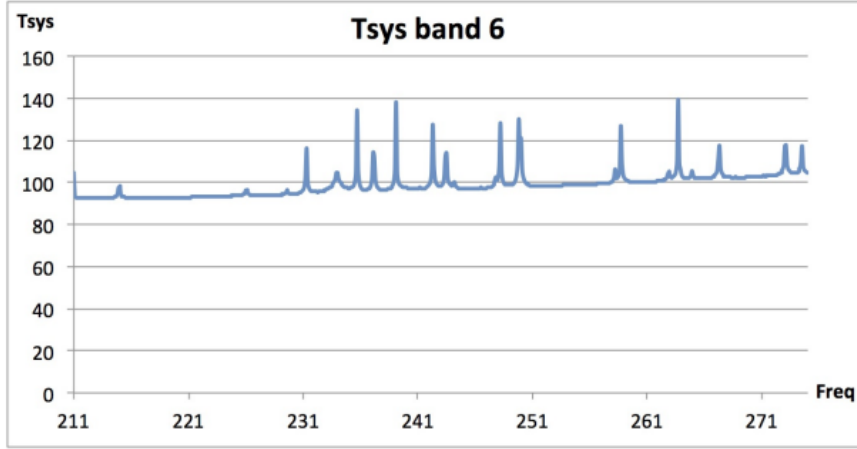


Figure 2.7: Typical T_{sys} at zenith for Band 6 with 1.262 mm PWV, based on measured values of the receiver temperatures.

The *system temperature* T_{sys} is defined as (e.g. Jewell et al. 1997, ALMA memo series):

$$T_{sys} = \frac{(1 + g)[T_{rx} + T_A(sky)]}{\eta e^{\tau_0 \sec z}}$$

where g represent the ratio of the gain response between the image and the signal, T_{rx} is the receiver noise temperature (of the order of 50 K over most of Band 6), $T_A(sky)$ is the antenna-based temperature of the sky, η is the antenna efficiency, related to the maximum antenna gain and to the antenna power pattern, τ_0 is the zenith optical depth of the atmosphere, $\sec z$ is the zenith secant which gives an estimate of the airmass at the observing elevation. The T_{sys} at Band 6 for PWV of 1.262 mm is shown in Figure 2.7.

Chapter 3

NGC 3100: ALMA Observations and Data reduction

This Chapter describes the ALMA observations obtained for NGC 3100 during Cycle 3 and the various step of the data reduction. The software used for data reduction and following analysis is CASA (Common Astronomy Software Application), version 4.7.0.

3.1 Observations

The observation of NGC 3100 was taken with the *12-m array* in Band 6 (~ 230 GHz) on March 22nd 2016 from 00:47:15.4 to 01:31:55.5 (UTC) with a total observing time of 44m 40s. 36 antennas were available and the array configuration had a maximum baseline of 460 m and a minimum baseline of 16 m. This corresponds to 0.65 arcsec of resolution and 10 arcsec of maximum recovered scale. Figure 3.1 shows the antenna configuration.

The used spectral configuration covered the frequency range 227 – 231 GHz and 240 – 244 GHz, divided in 4 SPWs:

- 3 SPWs of 128 channels with a total bandwidth of 2 GHz and a channel width of 15.6 MHz (~ 20 km/s)
- 1 SPW of 1920 channels with a total bandwidth of 1.87 GHz and a channel width of 0.98 MHz (~ 1.3 km/s)

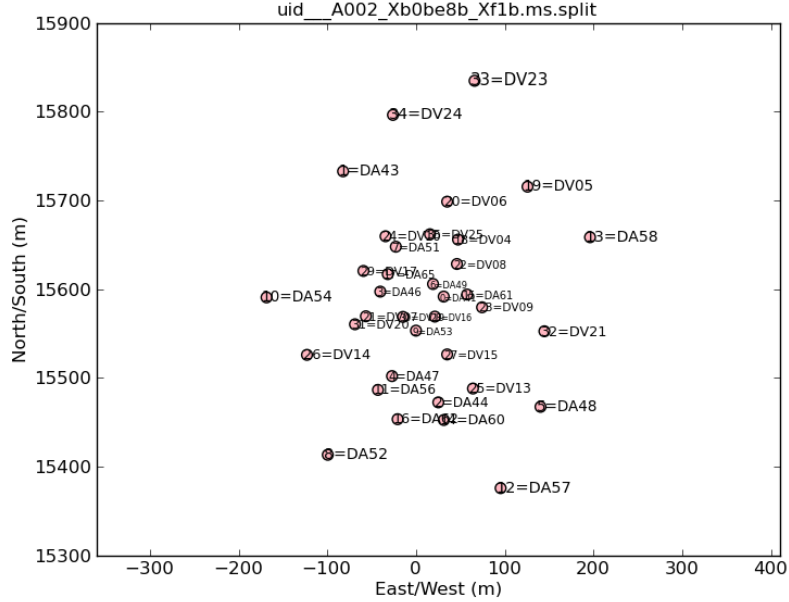


Figure 3.1: Antennas configuration. Distance is in meter; dots represent antennas.

The radio quasar J1037-2934 was used as bandpass, phase and flux calibrator. The amount of PWV range from 1.06 to 1.3 mm during the observations and the T_{sys} is $\sim 80 K$, on average.

3.2 Inspection and data calibration

3.2.1 CASA

Calibration, imaging and initial analysis of NGC3100 data were performed using CASA. This package has been developed to reduce interferometric data from modern radio telescopes such as ALMA and the upgraded VLA (or JVLA). It has a C++ core with an iPython interface. Its tasks and tools permit to deal with data from radio telescopes and to convert them in a so-called Measurement Set (MS). The MS has a table-based structure with main and sub-tables, in which all the information is contained.

The principal MAIN table is divided in three columns. The raw visibilities are contained in the DATA column, the calibrated and model visibilities are stored in the CORRECTED and MODEL columns, respectively. At the end of the calibration, these three columns are completely filled.

3.2.2 Data import, inspection and flagging

Raw data from ALMA were transformed in MS through CASA task **importasdm**. The so-called “a priori **flagging**” is applied on this MS. This editing removes data without specific inspection scan by scan. Data are identified and labelled based on the following reasons:

- *Shadowing*: depending on the elevation of the target, some antennas may obscure the ones behind them along the *LoS*, by reducing the effective collecting area. This flagging recognizes and labels the visibilities affected by shadowing.
- *Pointing*: during the observation some scans are taken to verify the accuracy of pointing, which must be more accurate at high frequencies. These data are not used.
- *Atmosphere*: as for pointing, some scans are used to calibrate the atmospheric effects during the observation.
- *Autocorrelation*: this is the result of the correlation of the signal of each antenna with itself. This flagging is necessary because noise due to systematic errors is amplified in autocorrelations and only cross-correlations between antennas are actually used.

3.2.3 A priori calibration

ALMA observations have to take into account two important factors related to the atmosphere and to the system noise: water vapour content and system temperature. In fact, the phase of visibilities are affected by the fluctuations in the troposphere, weather conditions and internal noise.

Fluctuations in the amount of PWV introduce a delay in baseline signals on short timescale (~ 1 s, see Section 2.2.3) that needs to be removed. This can be done thanks to the WVR mounted on each antenna that measures the amount of PWV during all the observation. In Figure 3.2 the effect of the WVR corrections antenna by antenna is shown.

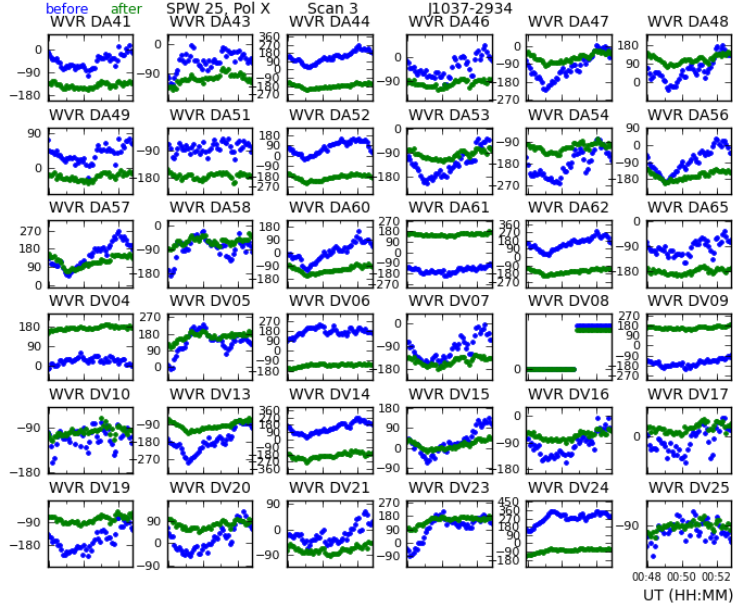


Figure 3.2: WVR corrections. The plots show the phase of the calibrator as function of time in SPW 3 in one polarization, for each antenna. Blue values are before WVR corrections, green values after them.

As seen in Section 2.2.4, the data are affected by the opacity of the atmosphere, by the antenna external temperature and by system noise. The corrections are taken into account through the T_{sys} calibration table. In Figure 3.3 it is possible to see how atmospheric effects on the visibilities were corrected by applying the T_{sys} table. In particular, it is possible to notice that the attenuation in correspondence of atmospheric lines disappear, and that the overall amplitude of the signal is rescaled.

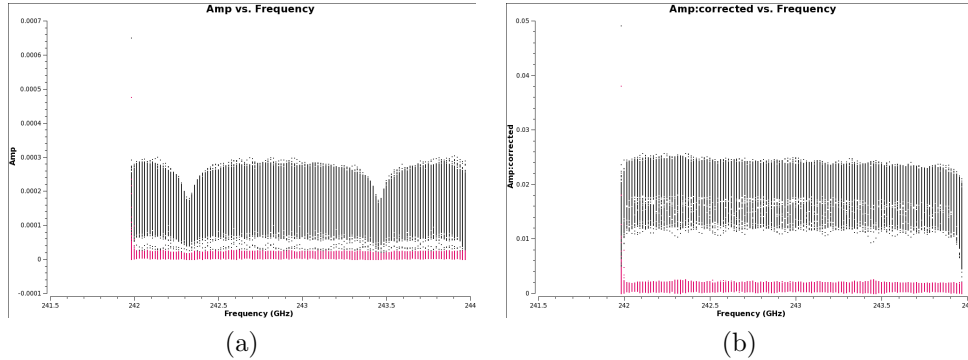


Figure 3.3: T_{sys} table corrections for SPW 2. (a) Visibilities amplitude vs frequency without applying the T_{sys} correction table. (b) The same with T_{sys} calibration table applied. Black lines are calibrator visibilities, while purple ones are NGC3100 visibilities.

After applying the WVR and T_{sys} tables, the MS was **split** in a new MS where only the target data are retained. Then, a new inspection of data allowed to identify possible corruptions in time and frequency. In particular, the edge channels of each SPW show high noise level during all observation. For this reason, the flagging of these channels was required.

3.2.4 Data calibration

The `setjy` task of CASA sets amplitude and phase for the flux calibrator, which is a source with known flux. This information is recorded in the MODEL column of the MS.

For the quasar calibrator J1037-2934, it was assumed a non-thermal model spectrum following

$$S = S_0 \left(\frac{\nu}{\nu_{rest}} \right)^\alpha$$

where $S_0 = 0.77 Jy$ is the specified flux density, $\alpha = -0.57$ is the spectral index and $\nu_{rest} = 234 GHz$ is the rest frequency.

Figure 3.4 (left panel) shows the model (amplitude vs uvdist) for all SPWs. The model results flat, because the calibrator is a point-like source, and the amplitude changes for each SPW, because the model spectrum considers their different central frequencies.

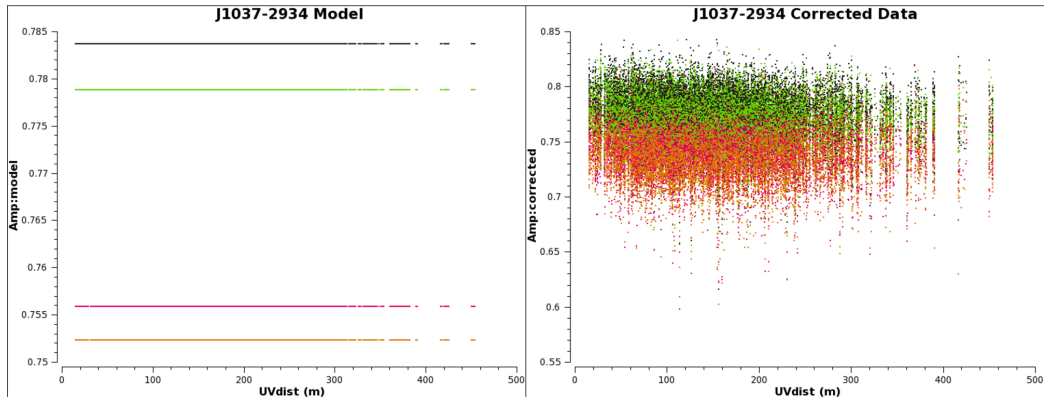


Figure 3.4: Model (on the left) and corrected data (on the right) for J1037-2934. Amplitude vs. uv distance. Different colors correspond to different SPWs.

The **Bandpass frequency-dependent** gains $B(\nu)$ correct for amplitude and phase as a function of frequency, and are computed averaging in time. For this reason, the bandpass calibrator visibilities are firstly corrected by a time-dependent table to avoid phase corruptions on short timescales for each channel. Besides, this gives statistically significant solutions and it prevents from signal decorrelation. A gain factor table that contains **short time-dependent** solutions is found and it is applied “on the fly” to bandpass visibilities. The bandpass solutions, stable in time, are computed by an all-scan time integration to maximize the SNR. The bandpass calibrator is usually a quasar (QSO), where spectral lines are absent, and it is observed at the beginning of the run. In this case the same calibrator was used for flux and bandpass calibration (J1037-2934).

The gain factor table that contains **long time-dependent** solutions $J(t)$ was found, using again J1037-2934 as calibrator. The source was regularly observed during the run, keeping it at the phase centre (so that it will have phase 0) in order to correct for atmosphere corruptions acting on phase and amplitude as a function of time.

These solutions are obtained using the CASA task **gaingal**.

Figure 3.5 shows two tables of gaincal solutions for amplitude and phase, respectively. The first one was obtained averaging the two polarizations, the second one was obtained for each polarization.



Figure 3.5: Solutions for (a) amplitude and (b) phase as a function of time. Each plot corresponds to a different antenna.

3.2.5 Data examination

The final result of data calibration can be seen in Figure 3.6, where the calibrator and the source are plotted in black and purple, respectively. As explained, the radio quasar J1037-2934 has been observed in different scans. The first scan of the calibrator is the longest because it was used for bandpass calibration. The others are intended for phase calibration.

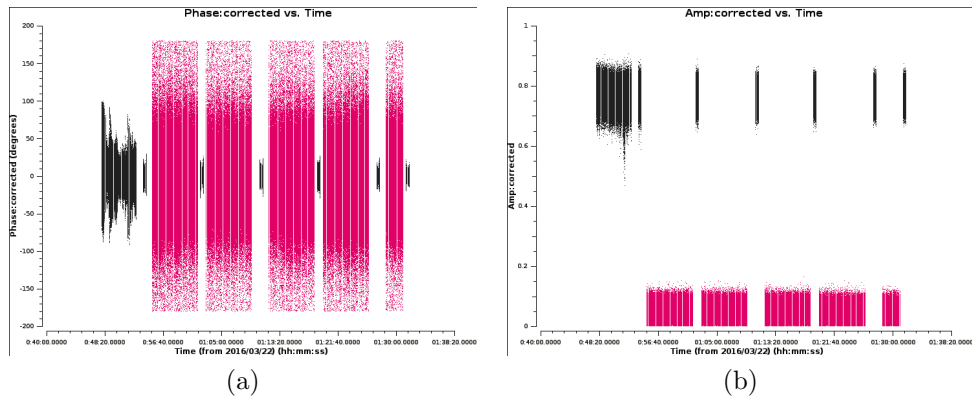


Figure 3.6: Corrected visibilities of J1037-2934 and NGC3100. (a) The phase of visibilities as function of time, averaged for all channels. (b) The amplitude of visibilities as function of time, averaged for all channels. The calibrator is in black, NGC3100 is in purple.

Figure 3.7 shows the calibrator amplitude and phase as a function of frequency. It can be noticed that the spread of the 1290-channels SPW is wider, both in amplitude and phase.

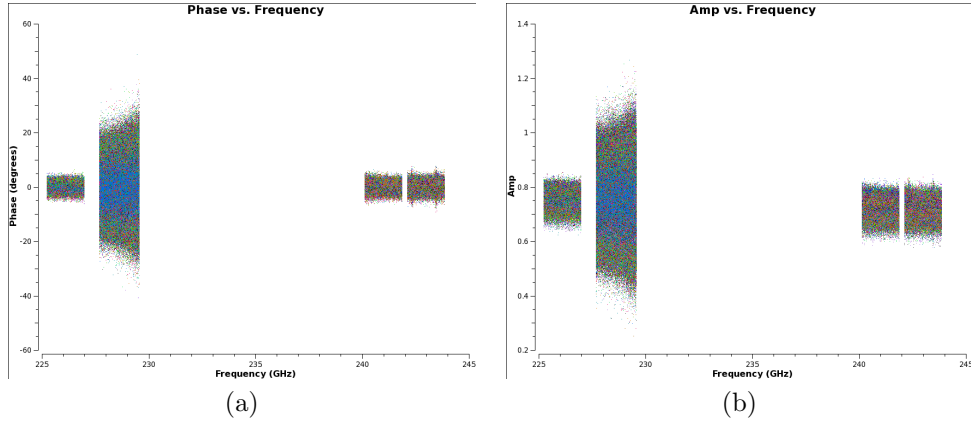


Figure 3.7: Corrected visibilities of J1037-2934. (a) Phase of visibilities as function of frequency, time-averaged. (b) Amplitude of visibilities as function of frequency, time-averaged. Plots are colourized by baselines.

Figure 3.8 shows the target NGC 3100 in the 1920-channel SPW. A double-horned line at the centre of the SPW is detected. The line is observed at ~ 228.5 GHz, corresponding to the CO(2-1) emission line ($\nu_{rest} = 230.5$ GHz) at redshift $z=0.0088$. The shape of the line suggests gas rotation.

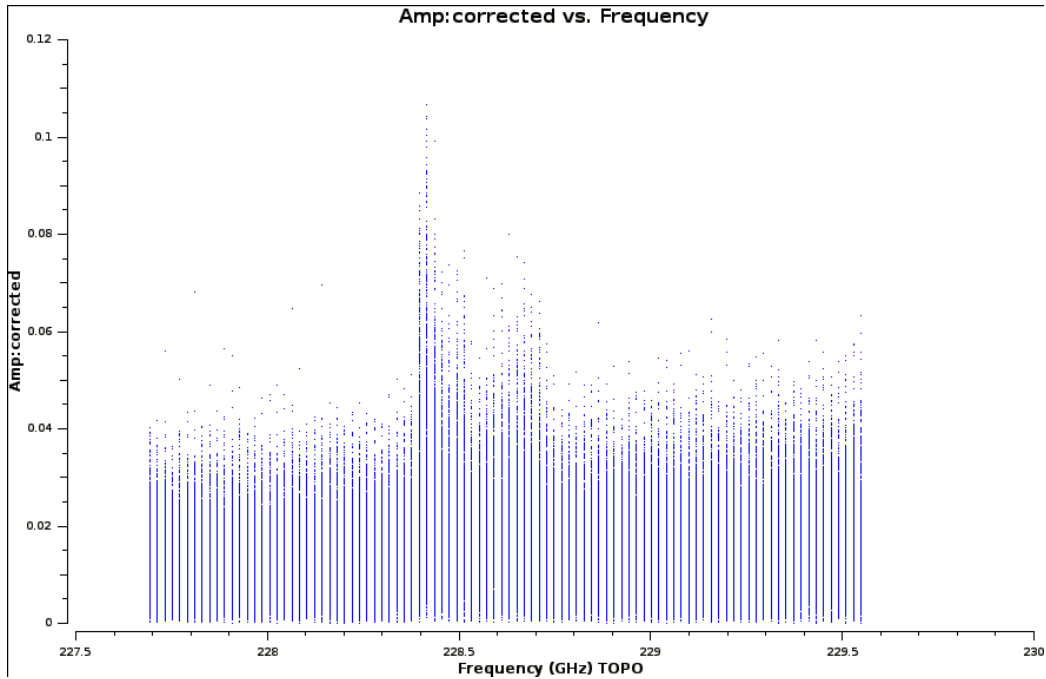


Figure 3.8: Corrected amplitude visibilities of NGC 3100 in SPW 3 as a function of frequency, time averaged. A double-horned line is detected in the centre.

3.3 Imaging

After the calibration, the data reduction continued through the **imaging** process.

3.3.1 Continuum image

A *continuum image* was obtained setting the *clean* mode to **msf** (Multi Frequency Synthesis) averaging all line-free channels. The central channels of SPW 3, from 228 to 229 GHz (where CO line is detected), and some channels of SPW 2 (high noise) were not considered for continuum imaging.

The obtained image has a beam of $0.98'' \times 0.71''$, a $RMS \sim 0.1 \text{ mJy beam}^{-1}$ and a flux peak of $0.025 \text{ Jy beam}^{-1}$.

The continuum image shows a jet starting from the centre of NGC 3100 and extending towards the South direction (Figure 3.9). The northern jet seen with the VLA (See Figure 1.5) is not detected.

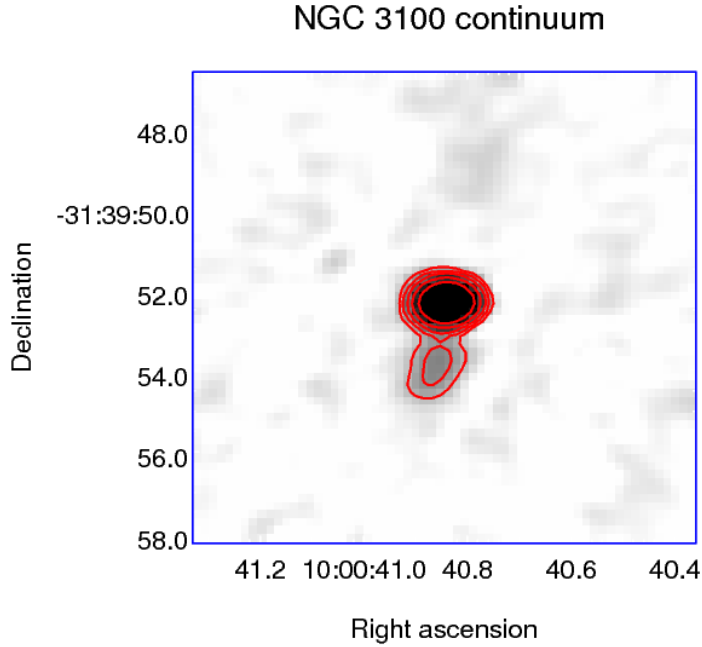


Figure 3.9: NGC 3100 continuum image. Resolution is 0.2 arcsec , noise level on the images is $0.1 \text{ mJy beam}^{-1}$. Contours from 4σ to 20σ with 10 levels.

Since this thesis is mainly focussed on the analysis of the CO line data cube, no efforts were attempted to obtain a better continuum image. Nevertheless, a more accurate *continuum image* of NGC 3100 was obtained through self-calibration by Ruffa et al. (in prep.). *Self-calibration* is a technique to refine the target source calibration. Instead of an external calibrator, a model of the target is used to calibrate itself.

Figure 3.10 shows the new continuum image where both jets are now detected.

The previous continuum image in Figure 3.9 was able to show only the southern jet, because of its high level noise ($\sim 0.1 \text{ mJy beam}^{-1}$). The self-calibration improves the RMS to $0.025 \text{ mJy beam}^{-1}$ and it makes both jets well visible.

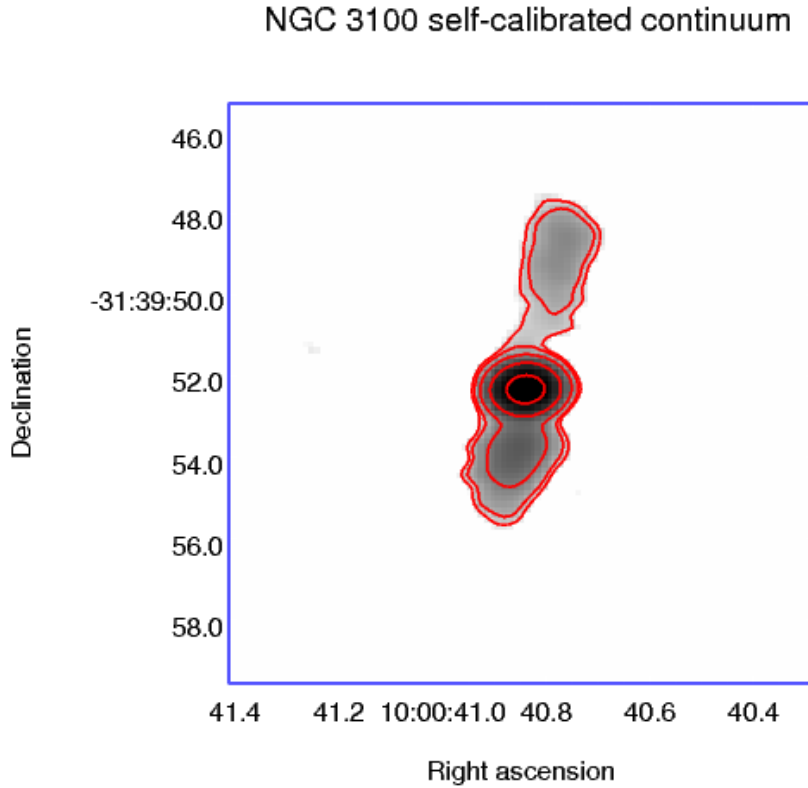


Figure 3.10: NGC3100 continuum image self-calibrated. Both jets are detected. Resolution is 0.14 arcsec, noise level on the images is $0.025 \text{ mJy beam}^{-1}$. Contours from 4σ to 20σ with 5 levels.

3.3.2 CO line Image

A *line image* can be obtained using the task `clean` in channel/velocity mode in order to get an image cube (*data cube*), containing a defined number of 2-D images along the frequency/channel axis.

After having applied the CASA task `uvcontsub` to subtract the continuum flux from data, a channel image was obtained using natural weighting and setting the spectral resolution to $\Delta\nu \sim 10 \text{ MHz}$ ($\sim 13 \text{ km/s}$). The resulting beam is $1.01'' \times 0.73''$; the noise level measured on an empty channel is $\sim 0.5 \text{ mJy beam}^{-1}$. Figure 3.11 shows that the double-horned line spectrum turns into a ring in the channel map. In particular, the ring has blueshifted emission in the north region and redshifted emission in the south region with respect to the system velocity of 2592 km/s.

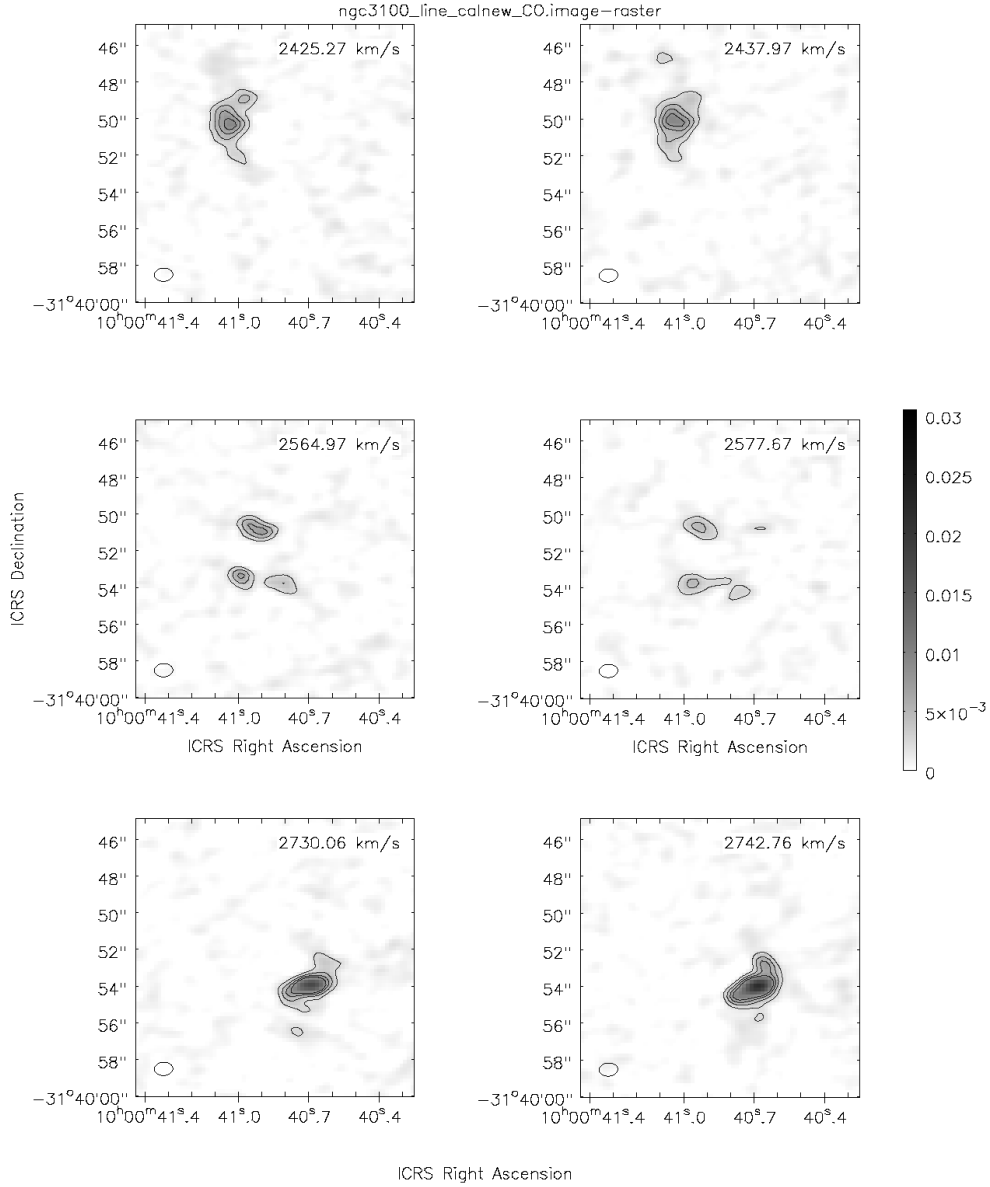


Figure 3.11: NGC3100 CO(2-1) line channel map. Spectral resolution is $\Delta\nu \sim 10 \text{ MHz}$ ($\sim 13 \text{ km/s}$), noise level is $\sim 0.5 \text{ mJy beam}^{-1}$. Contours from 4σ to 20σ with 5 levels.

The integrated intensity map of the line (moment 0) and the integrated velocity map (moment 1) were extracted from this map (See Chapter 4). Moreover, this is the map used as input for the modelling of the velocity field of the molecular gas discussed in Chapter 5.

Chapter 4

NGC 3100: Data Analysis

This thesis is focussed on the analysis of the CO properties of NGC 3100, but important information on the interpretation of the results may come also from comparisons with radio continuum and dust emission.

4.1 CO line Moment Maps

A *data cube* can be most easily thought of as a series of image planes stacked along the spectral dimension (See Section 3.3.2). It is possible to collapse the cube into a *moment* image by taking a linear combination of the individual planes $I(x_i, y_i, \nu_k)$:

$$M_m(x_i, y_i) = \sum_k^N \nu_k^m(x_i, y_i) I(x_i, y_i, \nu_k)$$

where x_i, y_i indicate the i -th pixel of the plane of frequency ν_k . The moments are computed using a *threshold* which defines the range of pixel values of the data cube to include in the resulting map.

The *integrated intensity map (moment 0)* M_0 can be written as:

$$M_0 = \sum_k^N I(x_i, y_i, \nu_k)$$

and roughly represents the amount of gas present in each pixel as derived by summing the contributions from all spectral planes (*column density*).

The map was produced with a threshold of 4σ , and a noise level of $\sim 0.3 \text{ Jy beam}^{-1} \text{ km s}^{-1}$ is measured (Figure 4.1).

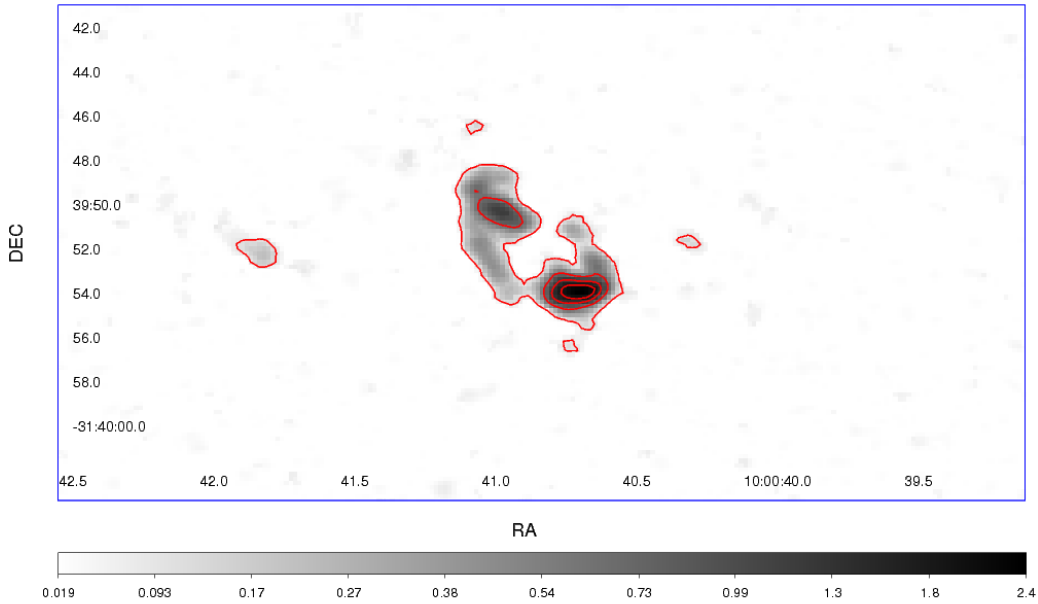


Figure 4.1: Integrated intensity map (moment 0). The RMS noise level is $\sim 0.3 Jy beam^{-1} km s^{-1}$. The wedge at the bottom shows the scale of the map in $Jy beam^{-1} km s^{-1}$. Contours from 4σ to 20σ with 5 levels.

The moment 0 map clearly shows the ring-like structure, already noticed in the channel maps. The major and minor axes of the ring are $\sim 8 \times 4 arcsec^2$ or $1.5 \times 0.75 kpc^2$. The ring appears inhomogeneous and even disrupted along the minor axis. Some additional emission is present outside the ring. This emission appears significant ($> 4\sigma$) and shows some correspondence with dust structures (See Section 4.3).

The *integrated velocity map (moment 1)* M_1 is defined as:

$$M_1 = \frac{\sum_k^N \nu_k I(x_i, y_i, \nu_k)}{M_0}$$

and represents the velocity field of the gas. It gives important information about the velocity range spanned by the gas and on the presence of velocity structures (i.e. the presence of preferred velocities at given positions).

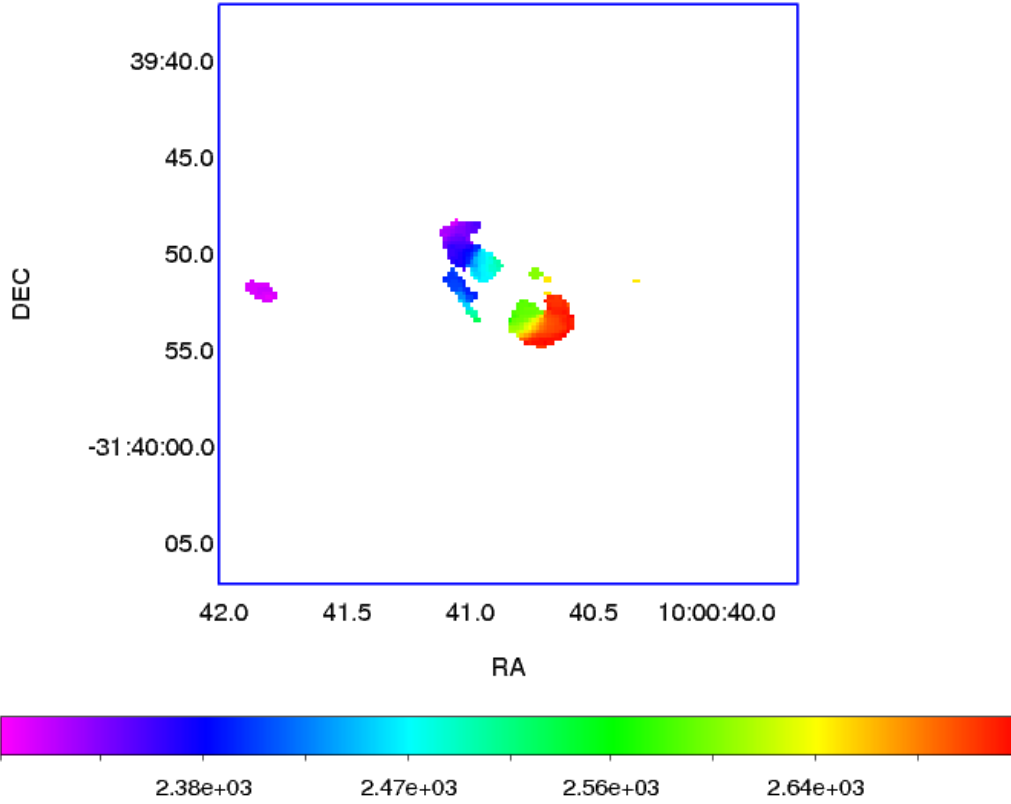


Figure 4.2: Integrated velocity map (moment 1). The range of velocity is $\sim \pm 200 \text{ km/s}$ around the $V_{sys} = 2592 \text{ km/s}$. The threshold is set at 4σ .

The moment 1 map was derived with a 4σ threshold and is presented in Figure 4.2. The gas is distributed in a rotating disk that can be roughly divided in two parts: an upper blueshifted part and a lower redshifted part (See Section 3.3.2). The velocity spans a range of $\sim \pm 200 \text{ km/s}$ around the systemic velocity (2592 km/s). However, some velocity irregularities seem to be present, perhaps indicating non-circular motions (See Section 5.2.4).

4.2 The CO as molecular gas tracer

The molecular gas mass in galaxies is dominated by molecular hydrogen, H_2 , but its strongly forbidden rotational transitions make it very difficult to directly detect it, unless shocked or heated to very high temperatures. For this reason, the emission from other molecules is usually used to trace the H_2 in galaxies (Carilli & Walter 2013). The carbon monoxide (CO) is

the most abundant molecule in the interstellar medium (ISM) after H_2 , and emits strong rotational transition lines (occurring primarily through collisions with H_2). Then, it can be considered as a “good” tracer of the molecular hydrogen.

The CO luminosity, L_{CO} , is usually used to compute the total molecular gas mass (dominated by H_2). It can be calculated from the CO moment 0 map. For NGC 3100 the integrated CO(2-1) line flux density was measured by summing the contributions from the five regions shown in Fig 4.3. This results in $S_{CO} = 42.82 \pm 9.04 \text{ Jy km s}^{-1}$.

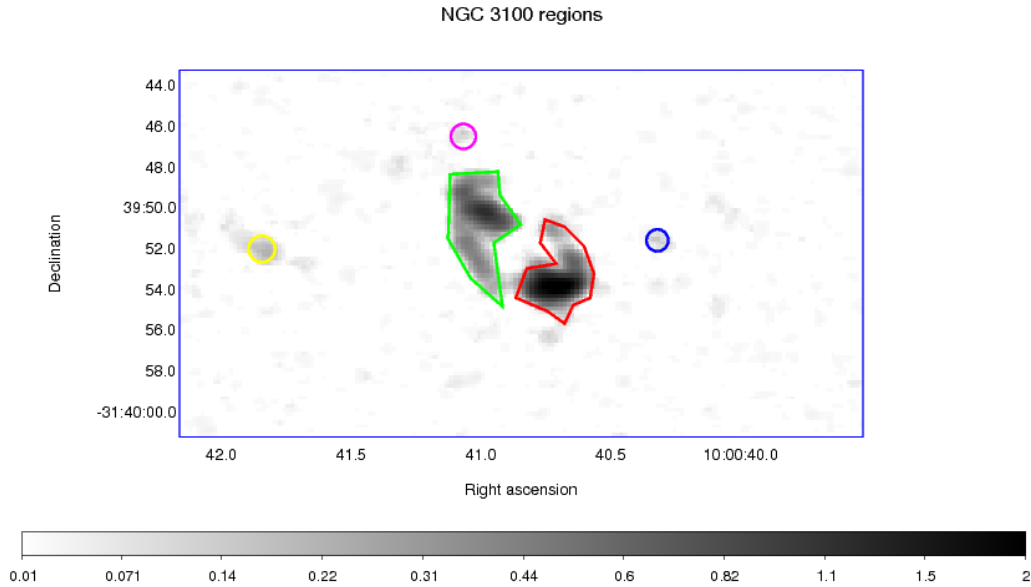


Figure 4.3: The five regions considered the measurement of the line flux density. a) in green, 11.48 arcsec^2 ; b) in red, 6.12 arcsec^2 ; c) in blue, 0.4 arcsec^2 ; d) in magenta, 0.64 arcsec^2 ; e) in yellow, 1.28 arcsec^2

Then, the luminosity L_{CO} can be derived as integrated source brightness temperature following Solomon & Vanden Bout (2005) equation:

$$L_{CO} = 3.25 \times 10^7 \left(\frac{S_{CO}}{\text{Jy km s}^{-1}} \right) \left(\frac{\nu_{obs}}{\text{GHz}} \right)^{-2} \left(\frac{D_L}{\text{Mpc}} \right)^2 (1+z)^{-3} \quad [K \text{ km s}^{-1} \text{ pc}^2]$$

where $\nu_{obs} = 228.77 \text{ GHz}$ is the observing frequency, $z = 0.0088$ is the redshift and $D_L = 40.9 \text{ Mpc}$ is the luminosity distance. The resulting CO luminosity is

$$L_{CO} = 4.3 \pm 0.9 \times 10^7 \quad [K \text{ km s}^{-1} \text{ pc}^2]$$

The CO luminosity- H_2 mass conversion equation is taken from Bolatto et al (2013):

$$M(H_2) = \alpha L_{CO} \quad M_\odot$$

where α is the so-called H_2 mass-to-CO luminosity conversion factor, defined as the ratio of the total molecular gas mass in M_\odot to the total CO line luminosity. Different source populations have different values of α , because α is strictly dependent on the molecular gas conditions, such as its density, temperature and kinetic state.

For NGC 3100 we used $\alpha = 4.3 M_\odot [(K km s^{-1} pc^2)^{-1}]$. The resulting mass is $M = 1.85 \pm 0.4 \times 10^8 M_\odot$, that is consistent with the mass computed from APEX observations ($M = 1.5 \pm 1.1 \times 10^8 M_\odot$, Laing et al. in prep), referring to a central 5 kpc region. This means that CO is mostly concentrated in the detected $1.5 \times 0.75 kpc^2$ ring.

We notice that the conversion factor used by Laing et al. was $X_{CO} = 2.3 \times 10^{20} cm^{-2} (K km s^{-1})^{-1}$, where X_{CO} is the conversion factor used to derive the molecular mass directly from the integrated fluxes. This value is very close to $X_{CO} = 2 \times 10^{20} cm^{-2} (K km s^{-1})^{-1}$, the value corresponding to $\alpha = 4.3 M_\odot [(K km s^{-1} pc^2)^{-1}]$ (Bolatto et al. 2013).

4.3 Comparison with dust and radio continuum

Figure 4.4 shows the dust absorption B-I image overlapped with the CO moment 0 map (red contours).

The CO ring-like structure nicely overlaps the inner semi-circular dust feature, suggesting the latter traces the same rotating structure. The other small detected CO regions do also tend to overlap with dust structures, suggesting the CO would trace the dust on much larger scales, but is not detected due to the fact that the present ALMA observations are not sensitive to scales larger than 10 arcsec (See Section 3.1).

NGC 3100 CO & Dust

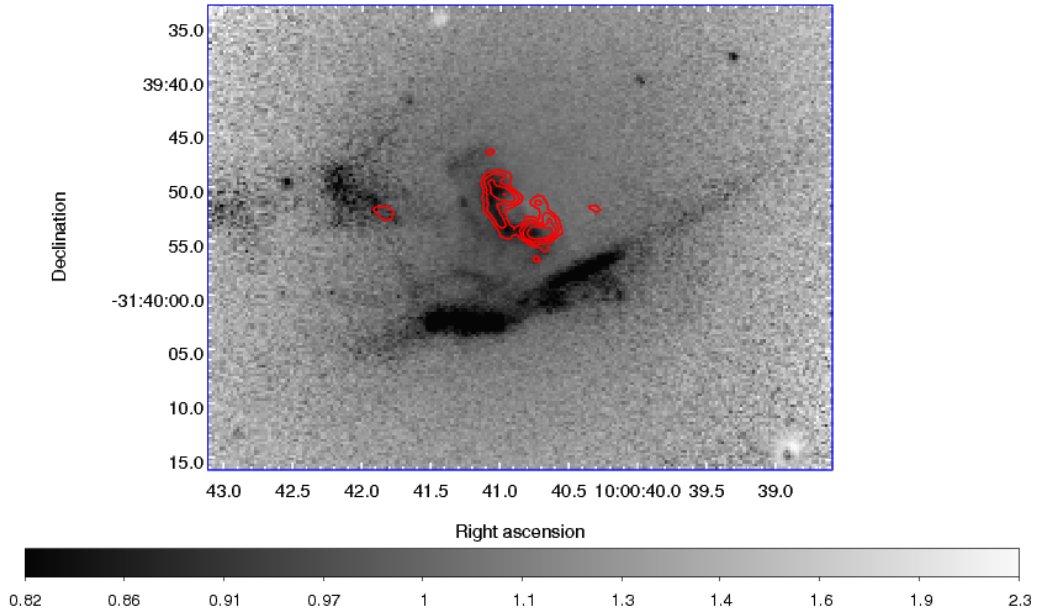


Figure 4.4: Moment 0 map over the B-I dust image. Contours from 4σ to 20σ with 5 levels.

The radio jets from the central AGN can affect the CO line emission. They could be responsible for the partial disruption that affects the CO ring. This is supported by Figure 4.5, which shows that the radio jet axis approximately coincides with the minor axis of the CO ring.

Indeed the jets seem to fill the areas of the CO ring from which flux is lacking. If interaction is present between the jets and the CO gas, it follows that the jet axis is not perpendicular to the CO disk.

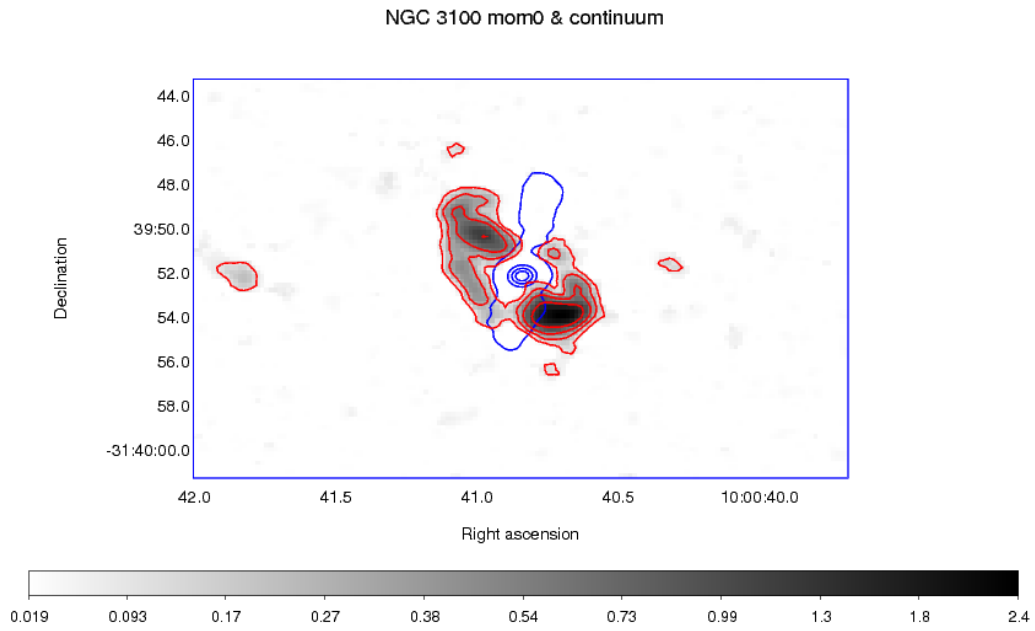


Figure 4.5: ALMA moment 0 map and continuum. Moment 0 in red, ALMA continuum in blue. Both contours start from 4σ to 20σ with 5 levels.

The ALMA radio continuum (230 GHz) is compared to three lower frequency observations from the VLA (5 and 8.5 GHz) in Figure 4.6.

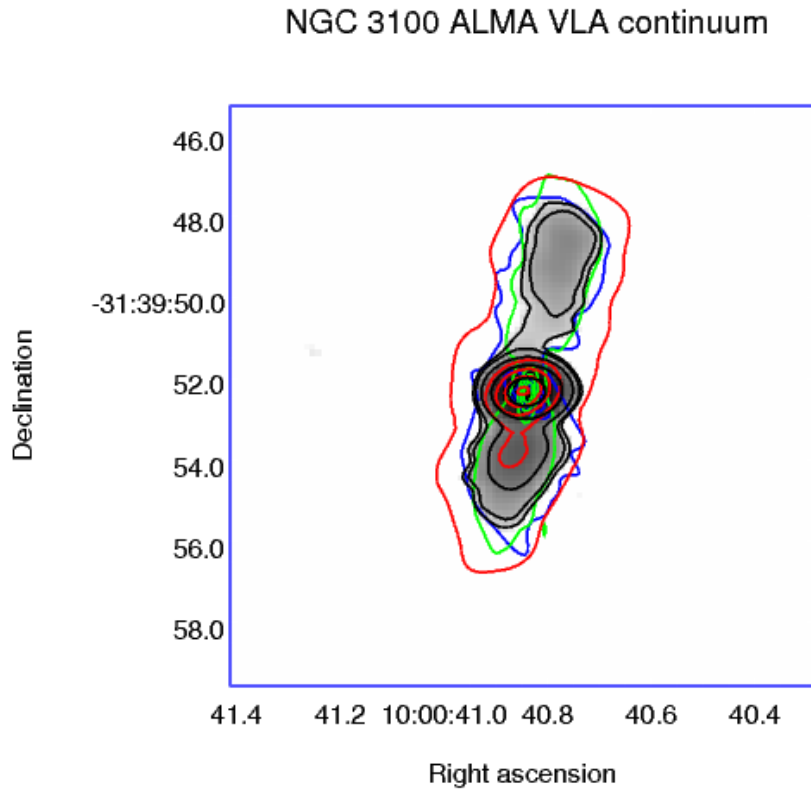


Figure 4.6: Continuum image of ALMA and VLA. Contours for ALMA (black) observations start from 4σ to 20σ with 5 levels. Contours for VLA observations start from 5σ to 25σ with 5 levels at 5 GHz (red and green) and from 4σ to 20σ with 5 levels at 8.5 GHz (blue).

The emission at each frequency shows a very good matching. By comparing the flux densities at the various frequencies, the spectral index of the various components can be inferred. As expected the core is flat, while the jets are steep ($\alpha = -0.7$).

Chapter 5

Kinematics modelling of the CO disk

To understand the kinematics and the morphology of the CO(2-1) rotating disk detected in NGC 3100, 3D models were built. The method chosen is the so-called *tilted-ring model*. Two softwares were used, **TiRiFiC** (Tilted Ring Fitting Code) and **3D-Barolo** (3D-Based Analysis of Rotating Object via Line Observations) working with different algorithms. The modelling strategy of the two programs will be briefly described and the final results will be shown.

5.1 Tilted-ring model

The so-called *tilted-ring model* was developed for the first time for observations of the neutral hydrogen (HI) emission-line (e.g. Rogstad & Shostak 1971) in the galaxy M83, to analyze the 2D velocity field in terms of a model consisting of hydrogen located in concentric rings rotating around the centre of the galaxy. The 2D *tilted-ring model*, also called *bending model*, is based on the assumption that the emitting material is confined to a disk and that the kinematics is dominated by the rotational motion (Rogstad et al. 1974). Each ring has a constant circular velocity $V_{rot}(R)$, depending only on the distance R from the centre. The disk is therefore broken down into a number of concentric rings with different radii, that can have different inclinations, position angles and rotation velocities (Figure 5.1).

TiRiFiC and 3D-Barolo developed a more complex 3D tilted-ring model.

In the 3D approach the full data cube is used to constrain the modeling (not only the 2D moment 1 maps). In addition instrumental effects are taken into account in the model through a convolution step. This has several

advantages; for instance it allows to remove artificial degeneracy between rotation velocity and velocity dispersion (e.g. line broadening). Unlike the 2D tilted-ring model, an analytic form for the fitting function in 3D does not exist and the model is instead constructed through Monte-Carlo extractions. Such techniques are known to be computationally expensive and they may converge to a local minimum of the function. In addition, a larger number of parameters is needed to describe the model with respect to the 2D case.

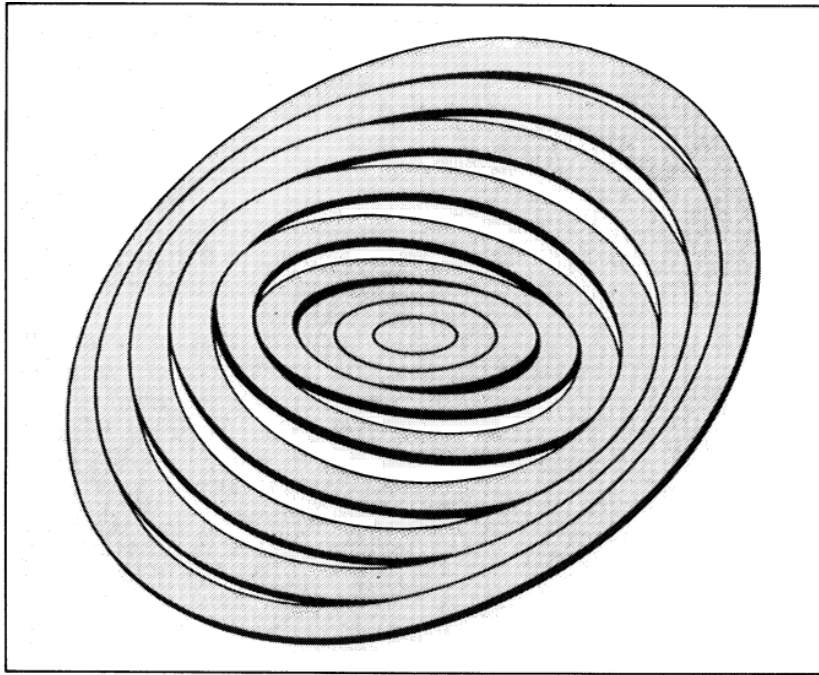


Figure 5.1: The bending model (Rogstad, 1974).

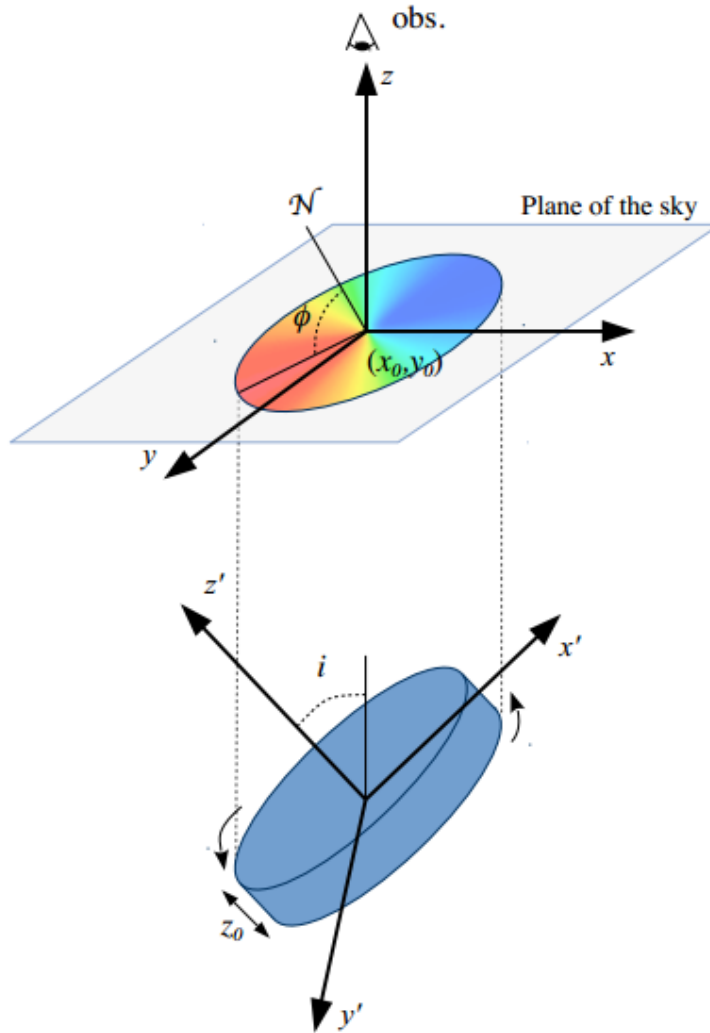


Figure 5.2: Geometrical parameters of the 3D disk model. The disk in the $x'y'z'$ space is projected into an ellipse in the xy plane of the sky. The inclination angle i is taken with respect to the plane of the sky, the position angle ϕ identifies the position of the major axis on the receding half of the disk and it is taken counterclockwise from the North direction

The 3D disk model is described by the following parameters (for each ring of radius R and width W , see Figure 5.2):

- spatial coordinates of the centre (x_0, y_0) ;
- systemic velocity V_{sys} ;

- inclination angle i with respect to the plane of the sky (90° for an edge-on galaxy).
- position angle ϕ , the angle of the ring major axis (taken on the receding side of the disk), defined counter-clockwise (i.e. moving to the East) from the North direction;
- rotational/circular velocity V_{rot} ;
- radial velocity V_{rad} for non circular motions;
- velocity dispersion σ_{gas} (only in 3D-Barolo);
- face-on (inclination corrected) surface brightness Σ ;
- scale-height of the gas layer z_0 .

All these quantities are allowed to vary for each ring.

TiRiFiC defines also a number of global parameters:

- the global isotropic velocity dispersion, which includes the instrumental dispersion;
- the vertical distribution of the gas density;
- the constant total flux of a single point source.

TiRiFiC rings

As mentioned above, in *TiRiFiC* (Józsa, 2007) the tilted-ring model is specified by parameters that vary with radius and global parameters. The parameters belonging to a given radius are referred to a “ring”, whose total number is defined by the user. A number of “sub-rings” with a user-specified width is created by linear interpolation of the ring-specific parameters. A Monte-Carlo integration is used to model these sub-rings in such a way that they rotate with the same tangential velocity and with a same orientation with respect to the observer, determined by the position angle and inclination. The resulting velocities are then projected onto a cube with dimensions set by the input data cube. After calculating a point-source model defined by clouds and after gridding the Monte-Carlo point sources onto a model cube, the cube is convolved with a 3D-Gaussian, a product of a 2D Gaussian in the image plane (xy plane) and a 1D Gaussian determined by the global velocity dispersion. The form of the Gaussian in the image plane is determined by the observing beam of the input cube (the CLEAN beam), which can be redefined by the user.

3D-Barolo rings

Unlike TiRiFiC, which has been mainly developed to study local galaxies with a detailed description of peculiarities, such as warps, spiral arms and lopsidedness, *3D-Barolo* (E. Di Teodoro & F. Fraternali, 2015) is designed to work also on low-resolution data, where the kinematic information is largely biased by the size of the beam.

The rings are directly formed by gas clouds (without defining sub-rings) with cylindrical coordinates that have a randomly and uniformly chosen radius R_c (with $R - W/2 < R_c < R + W/2$, where W is the ring width defined by the user) and an azimuthal angle θ_c ($0 \leq \theta_c \leq 2\pi$), and a height z_c above the plane of the disk, selected as a random deviate from a given vertical distribution of the gas density (z_0). As the sub-rings of TiRiFiC, the position of the clouds is then rotated and projected onto the plane of the sky with a given orientation with respect to the observer, according to the position angle and inclination at that radius. Then, the observed velocities along the *LoS* are calculated as a combination of systemic, rotational and random motions. The velocity profile at each location is related to the average velocity by dividing the clouds into a number of sub-clouds. The velocities are distributed as a Gaussian with dispersion $\sigma^2 = \sigma_{gas}^2 + \sigma_{instr}^2$, where σ_{gas} is the intrinsic gas dispersion and σ_{instr} the instrumental broadening. These velocities are then discretized and the contribution of the sub-clouds is recorded in a model cube with the same sizes of the data-cube.

5.1.1 Fitting algorithms: an overview

- **TiRiFiC method**

The fitting process in TiRiFiC provides best estimates for a subset of the disk geometrical parameters with the goal to get a simulated observation that optimally matches a real (input) observation. The method adopted to numerically determine the model quality is the χ^2 , altered by defining boundary conditions (minimum and maximum values for a parameter, regularisation schemes). Currently, the TiRiFiC optimisation aims at the minimisation of the χ^2 .

- **3D-Barolo method**

For each ring R , the algorithm builds a 3D model, convolves it with the observational beam and compares it with the data. If no convergence is achieved, 3D-Barolo updates the parameters and starts over. When the algorithm converges to the minimum, it moves to the next ring.

3D-Barolo allows the code to exclude one parameter from the fit, namely the surface density Σ of the gas. This process is referred to as *normalization*. Two different kinds of normalization are implemented: pixel-by-pixel and azimuthally averaged. We will refer to the first normalization as “local”. In this case the model is normalized in such a way that the column density maps of model and observations are the same. It avoids regions, such as areas with strong and clumpy emission or holes, that might affect the global fit (e.g. Lelli et al. 2012). In the second normalization the model is normalized to the azimuthal-averaged flux in each ring. This is useful to determine the inclination angle of the outer rings. The optional normalization step takes place after the convolution step.

TiRiFiC and 3D-Barolo algorithms can be summarized in two flow diagrams as shown in Figure 5.3.

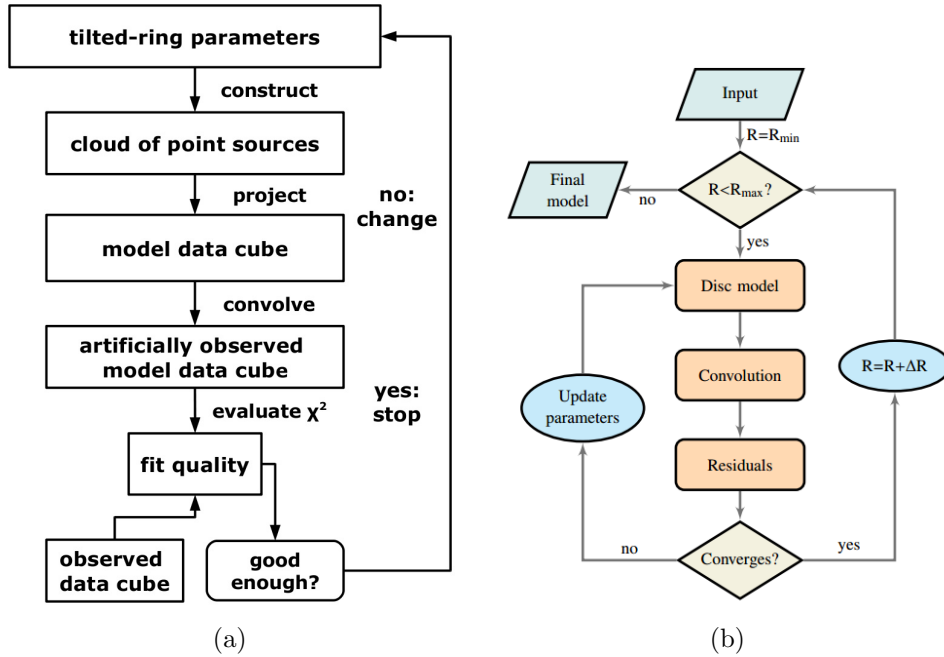


Figure 5.3: (a) TiRiFiC model construction and fitting. (b) 3D-Barolo model construction and fitting

The two softwares use two different methods of evaluation of **residuals**:

- *TiRiFiC* determines the quality through the χ^2 using the formulas

$$\chi^2 = \sum_k \frac{(M_k - D_k)^2}{\sigma_k^2} = \sum_k \frac{(M_k - D_k)^2}{w_k^2}$$

where k is an index running over all pixels in the cube, M_k is the model data cube, D_k the data, σ_k the noise of the original data cube in the k -th pixel, w_k the weight of a pixel. This can be written as:

$$w(k) = \sigma_{rms} + (\sigma_k^q)^2$$

where σ_{rms} is the rms noise of the original data cube and σ_k^q the quantisation noise of the convolved artificial data cube, taken into account by TiRiFiC.

- *3D-Barolo* calculates the residuals by comparing the model and the data pixel-by-pixel. The number F , used by the minimization algorithm, defines whether a model is suitable or not. It is the averaged sum of the residuals:

$$F = \frac{1}{n} \sum_{i=1}^n \Delta r_i w(\theta_i)$$

where n is number of pixels where the residuals Δr are evaluated and $w(\theta)$ is a weighting function. Three types of residuals can be provided:

$$\Delta r = \frac{(M - D)^2}{\sqrt{D}} \quad (1)$$

$$\Delta r = |M - D| \quad (2)$$

$$\Delta r = \frac{|M - D|}{(M + D)} \quad (3)$$

where M and D are the flux values of the model and the data, respectively. The residual defined by eq. (1) is a kind of χ^2 without however a conventional statistical meaning. When D is a blank pixel, D is set equal to the root mean square value (rms) of the cube. The residual defined by eq. (3) gives more weight to regions where the emission is faint and diffuse, the residual defined by eq. (2) is an intermediate case.

Residuals from TiRiFiC and 3D-Barolo are shown to the user during the fitting process, but they are not stored in output files.

5.2 NGC 3100 models

5.2.1 Model assumptions

Our ALMA observations clearly show that the CO is organized in a central disk/ring-like structure in NGC 3100, but the disk position angle and inclination are not known. Assumptions on these parameters must be made to proceed with a reliable modelling.

Both TiRiFiC and 3D-Barolo (hereafter referred to as Barolo) are able to create models without providing any specific constraints, but this increases the number of free parameters and could bring to a degeneration in the model and to high residuals.

TiRiFiC has a large number of optional parameters, but systematic errors can be reduced by setting the maximum range allowed for each parameter. Setting sensible ranges for the parameters can improve the model.

Barolo cannot handle ranges, but the number of parameters is limited.

The following assumptions were made to build the models with both TiRiFiC and Barolo:

- The *spatial coordinates of the centre* (x_0, y_0) were set by examining the data cube and *moments*.
- The *systemic velocity* V_{sys} was taken from the data.
- The *scale height* z_0 was set at 0.02 arcsec . This means that we are assuming a bidimensional disk.

These parameters were fixed once for ever and not allowed to vary in the fitting process.

- The first guess *face-on surface brightness* Σ in TiRiFiC was set by measuring the mean emission of the disk in the data image. 3D-Barolo required no input for Σ .

The position angle ϕ and the inclination i were found through different tests with Barolo, in which these parameters were set to a number of values. Firstly, the best ϕ was found by visually matching the modeled disk with the actual flux distribution in the moment 0 image.

- The best *position angle* ϕ turned out to be 227° .

We set the value of the inclination i in a similar way. Four models with different i were built, all with $\phi = 227^\circ$. Figure 5.4 shows the i values that best match the actual flux density distribution: $i = 60^\circ$ and $i = 55^\circ$.

- The *inclination* $i = 60^\circ$ was finally chosen. This choice was motivated by the fact that the modeled disk is bidimensional, while the real one must have a finite (> 0) height. This means that the emission in the disk coming from different heights and seen in projection on the sky plane, is modeled as being part of the disk plane causing a broadening of the modeled disk size. To correct for this effect, a higher inclination values is chosen, meaning a smaller (more realistic) projected disk size.

At this point ϕ and i were fixed to their best values and not allowed to vary in the fitting process.

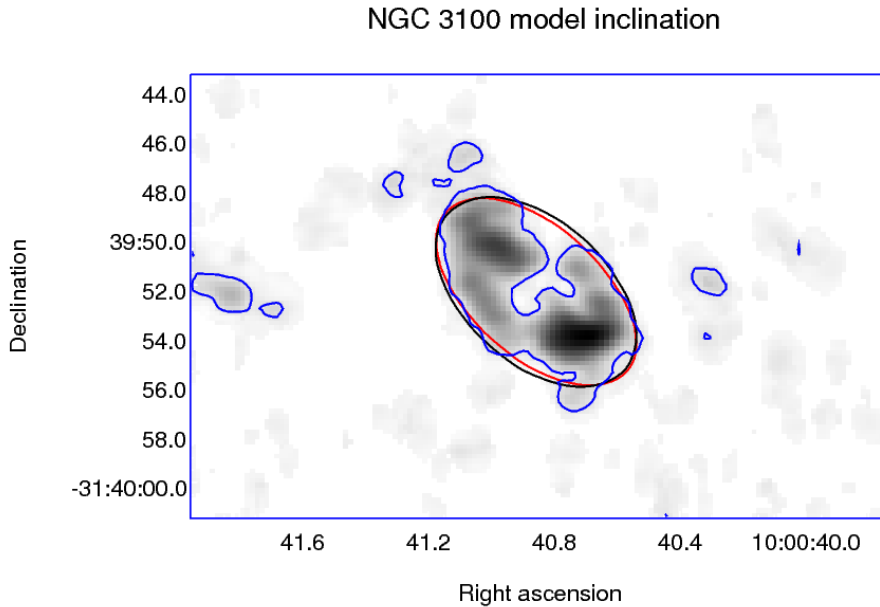


Figure 5.4: Inclination of the model. Contours for the input data cube (in blue), from the model at $i = 55^\circ$ (in black) and the model at $i = 60^\circ$ (in red). Each contour is at 3σ assuming σ from the input data.

The moment 0 map of NGC 3100 shows inhomogeneities and distortions that may hint towards a warped structure. Because of this, it would be better to let ϕ vary along the disk, i.e. to assume ϕ as free parameter. Features similar to warps in the moment 0 map could also be produced by a complex velocity field i.e. non-circular motions, described by the radial velocity V_{rad} parameter. The typical signature of non-circular motion is a tilt of the isovelocity contours with respect to the geometrical principal axes (Figure 5.5).

Due to this degeneracy between V_{rad} and ϕ models taking into account variations of only one of this two parameters were explored. In particular, we decided to fix ϕ and let V_{rad} vary. This is supported by the fact that deviations from regular rotation are visible in the moment 1 map. This is nicely shown in Figure 5.6, where the moment 1 map was created (by Barolo) in a different way with respect to the one shown in Figure 4.2. In this case the pixels were not masked using a general threshold (4σ), but applying a smoothed mask to the data cube, after degrading it to lower resolution. This

means that lower surface brightness features are retained. This moment 1 map shows tilted velocity structures near the centre.

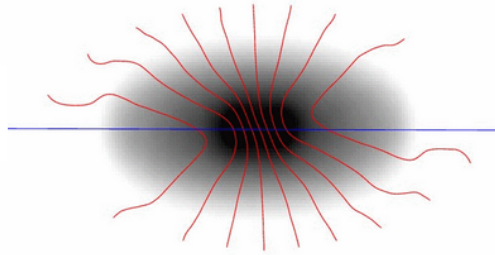


Figure 5.5: Velocity field of a rotating disk with additional non-circular motion. The typical signature is a tilt of the isovelocity contours with respect to the geometrical principal axes.

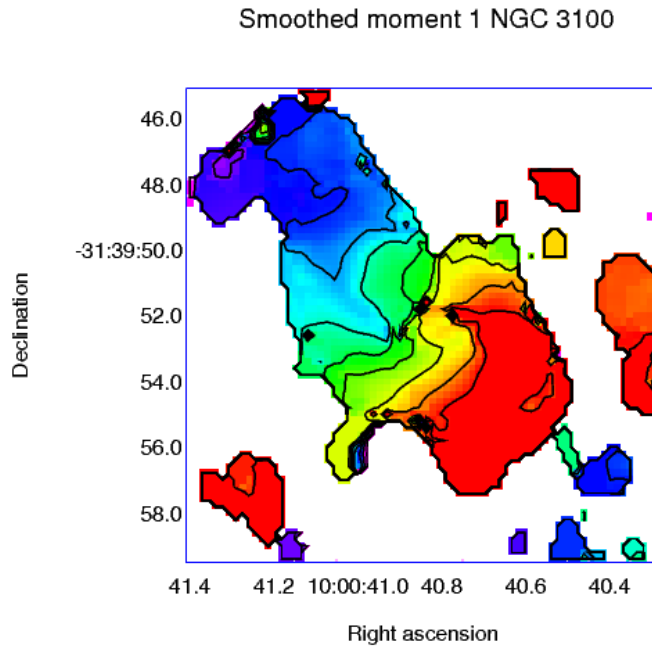


Figure 5.6: Moment 1 map obtained by applying a smoothed mask to the data. Contours from $V = 2300 \text{ km/s}$ to $V = 2726 \text{ km/s}$ with $V_{sys} = 2592 \text{ km/s}$.

Two different models were produced: a pure rotational one, and a model including non-circular motions. This was done with both Tirific and Barolo. Table 5.1 shows the ϕ and first guess V_{rad} values used to produce the models described in Section 5.2.2.

Model	Parameter	TiRiFiC	3D-Barolo
<i>Rotational</i>	ϕ [°]	227	227
	V_{rad} [km/s]	–	–
<i>Non-circular</i>	ϕ [°]	227	227
	V_{rad} [km/s]	50	50

Table 5.1: List of the models obtained with TiRiFiC and 3D-Barolo. The models can be divided in purely “rotational models” and “non-circular models” where non-circular motion (V_{rad}) has been added.

5.2.2 TiRiFiC models

The models produced by TiRiFiC are obtained through a two-step fitting process. The geometrical parameters obtained from the first fitting are edited and used as inputs for the second fitting.

In the input file, a disk composed of 11 rings separated by 0.5 arcsec was defined. The disk was decomposed in two semi-disks with the same fixed and first guess parameters. The fixed parameters are set as described in Section 5.2.1. The first guess for the face-on surface brightness Σ was set to $0.05 Jy km s^{-1} arccsec^{-2}$ and the first guess for the rotational velocity V_{rot} was $100 km/s$.

To make solutions more stable, some parameters are not fitted independently for each ring, but only for each even ring. Intermediate values are interpolated.

Figures 5.7 and 5.8 show the output disk parameters for the purely rotational model and the non-circular one respectively. It is worth noticing that in its present implementation TiRiFiC is not able to evaluate parameter errors. So these plots should be interpreted with caution. In particular we do not consider as reliable the first and the last of the plotted points, that refer to regions where the emission is detected at low SNR (see Schmidt et al. 2014 for more details).

Both models show a clear peak in the surface brightness (indicate in the plots as SBR) at a radius $r \sim 3 \text{ arcsec}$ and, as expected, a raising rotational velocity going toward larger distances from the center. The absence of error bars makes it impossible to establish if the $\sim 50 \text{ km/s}$ V_{rad} peak seen at $r \sim 3 \text{ arcsec}$ in Figure 5.8 is significant.

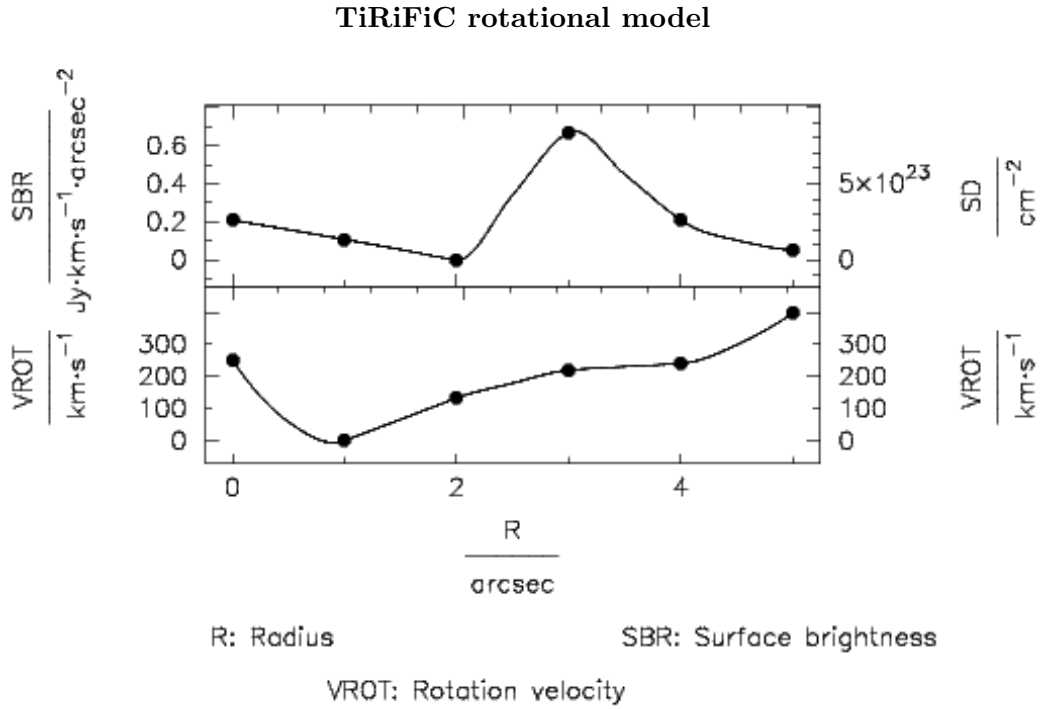


Figure 5.7: TiRiFiC best-fit disk parameters of purely rotational model.

TiRiFiC non-circular model

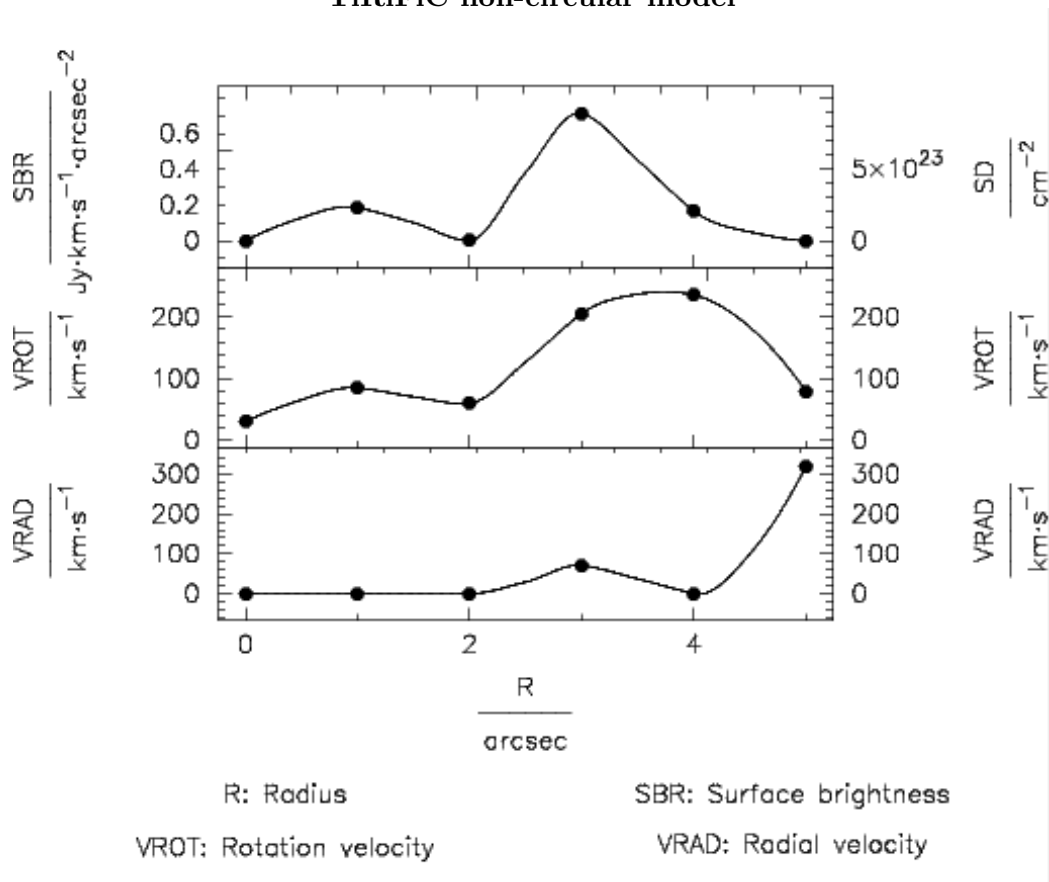


Figure 5.8: TiRiFiC best-fit disk parameters of non-circular model.

The comparison between the data and the two best-fit models is shown in Figure 5.9 and 5.10 respectively, through fifteen representative channel maps. The non-circular model seems to better reproduce the data in the central velocity channels than the purely rotational model.

A similar behaviour is seen in the Position-Velocity (PV) plots shown in Figure 5.11. Both models roughly reproduce the data along the major axis (at least in the external regions, upper panels), while the non-circular model provides a clearly better result along the minor axis (lower panels).

TiRiFiC rotational model

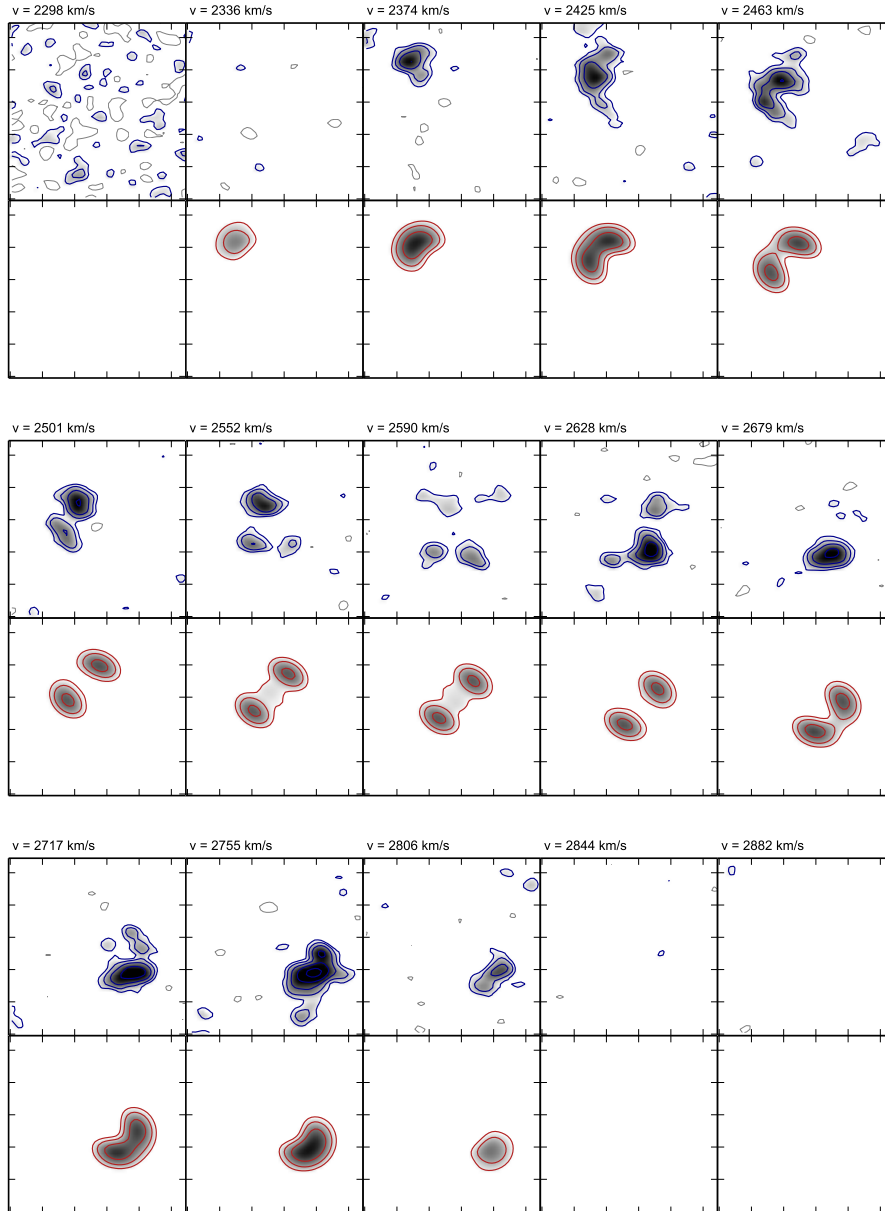


Figure 5.9: Comparison between the data (blue, top panels) and the rotational model (red, bottom panels) in fifteen representative channel maps. The contours start from 2.5σ , negative contours are shown in grey.

TiRiFiC non-circular model

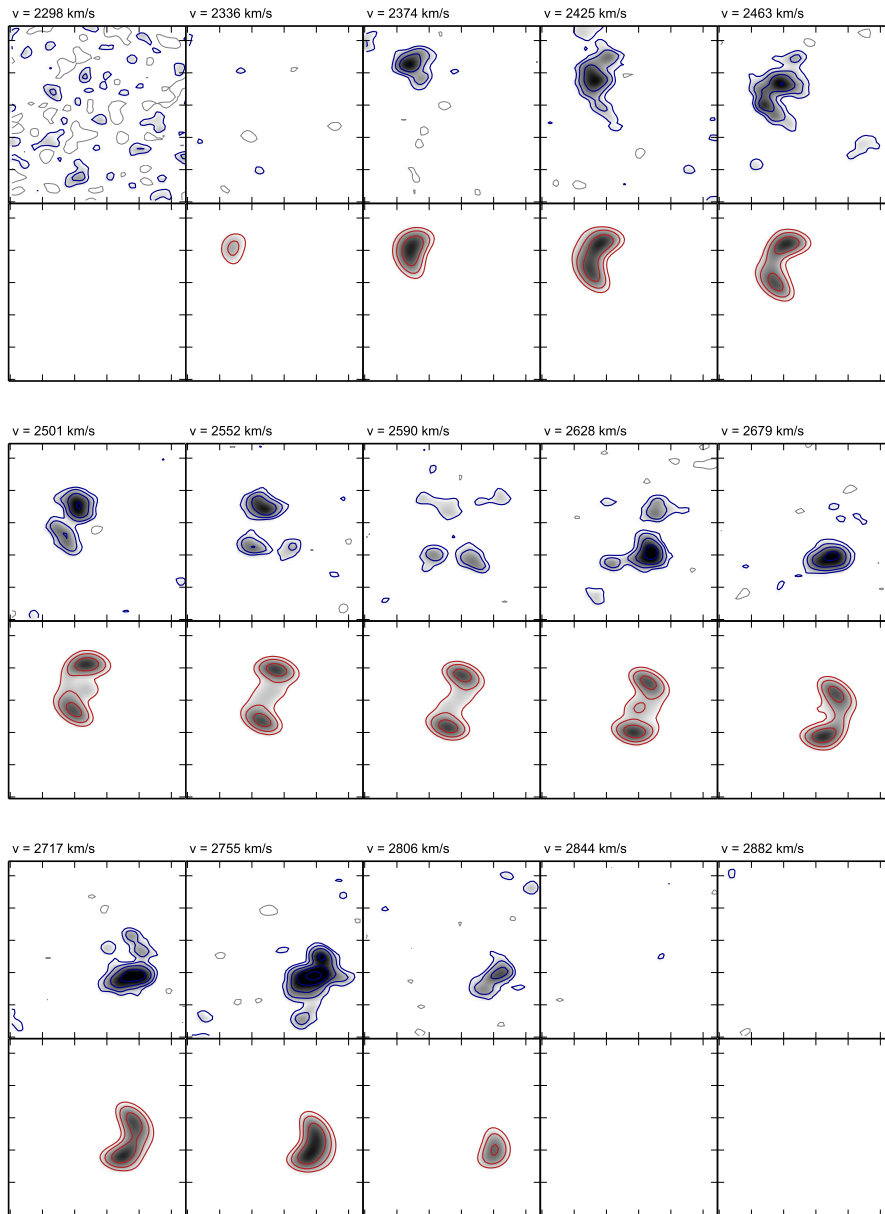


Figure 5.10: Comparison between the data (blue, top panels) and the non-circular model (red, bottom panels) in fifteen representative channel maps. The contours start from 2.5σ , negative contours are shown in grey.

TiRiFiC position-velocity diagrams

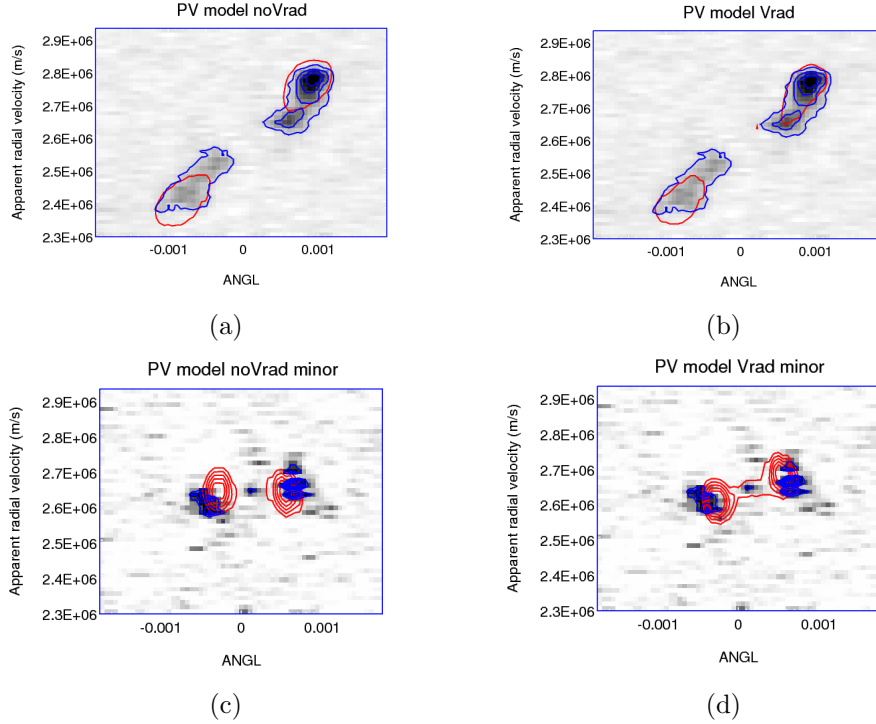


Figure 5.11: Position-velocity diagrams along the major axis for the (a) rotational and (b) non-circular models. Position-velocity diagrams along the minor axis for the (c) rotational and (d) non-circular models. Data are shown in grey-scale and blue contours, the models in red.

5.2.3 3D-Barolo models

In this section the rotational and non-circular models produced by Barolo are presented. In Barolo we were able to use both the local and azimuthal normalizations (See Section 5.1.1).

As in TiRiFiC, a disk composed of 11 rings separated by 0.5 arcsec was defined. The same assumptions of Section 5.2.1 are made for the parameters, whose values are fixed at the beginning and are not allowed to vary in the fitting process, and the same first guess values are given for variable parameters. In this case all rings are independently fitted and no interpolation is done.

Figure 5.12 and 5.13 show the best-fit disk parameters for the purely rotational and the non-circular models respectively. Both azimuthal (upper panels) and local (lower panels) normalizations are shown. In addition to velocities (rotational and radial), Barolo produces a best-fit also for the ve-

locity dispersion (σ_{gas}). A plot for the surface brightness is also produced by Barolo, even if no input parameter are given (Figure 5.14). Moreover Barolo is able to estimate errorbars, making the interpretation of these plots much more reliable.

The disk parameters obtained with Barolo are all very similar to each other for both models and normalizations and also very similar to the ones obtained with Tirific (a direct comparison between Barolo and TiRiFiC can be done only for the azimuthal normalization). All Barolo models show a flattening of the rotation curve at $r < 2 \text{ arcsec}$ (which appear significant), similar to the flattening shown by the non-circular TiRiFiC model. As for TiRiFiC, Barolo V_{rad} values are all consistent with zero, except perhaps for the value around $r \sim 3 \text{ arcsec}$. In this case however the estimated velocity is $\sim -50 \text{ km/s}$. This is due to a different velocity direction convention between Barolo and Tirific.

The comparison between data channels and the two best-fit models (rotational and non-circular) is shown in Figure 5.15 - 5.18 for both normalizations.

By definition models with local normalization better represent the data than those with azimuthal normalization. Differently from TiRiFiC, Barolo non-circular models do not show an appreciable improvement in the central channels with respect to purely rotational models, which already provide a reasonably good fit to the data.

3D-Barolo rotational model parameters

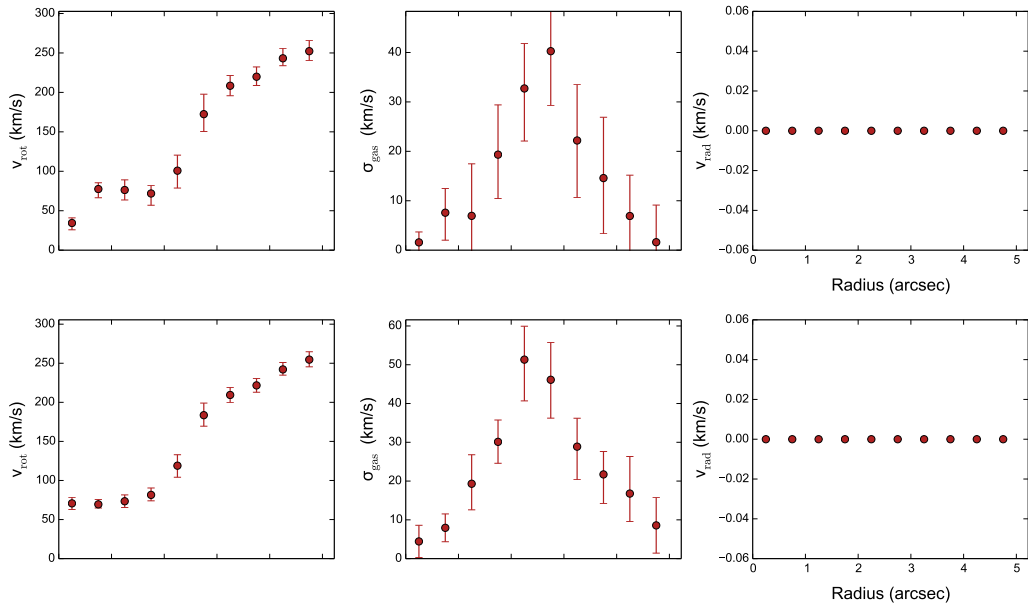


Figure 5.12: Parameters of the disk for the azimuthal (upper panels) and “local” (lower panels) purely rotational models of 3D-Barolo.

3D-Barolo non-circular model

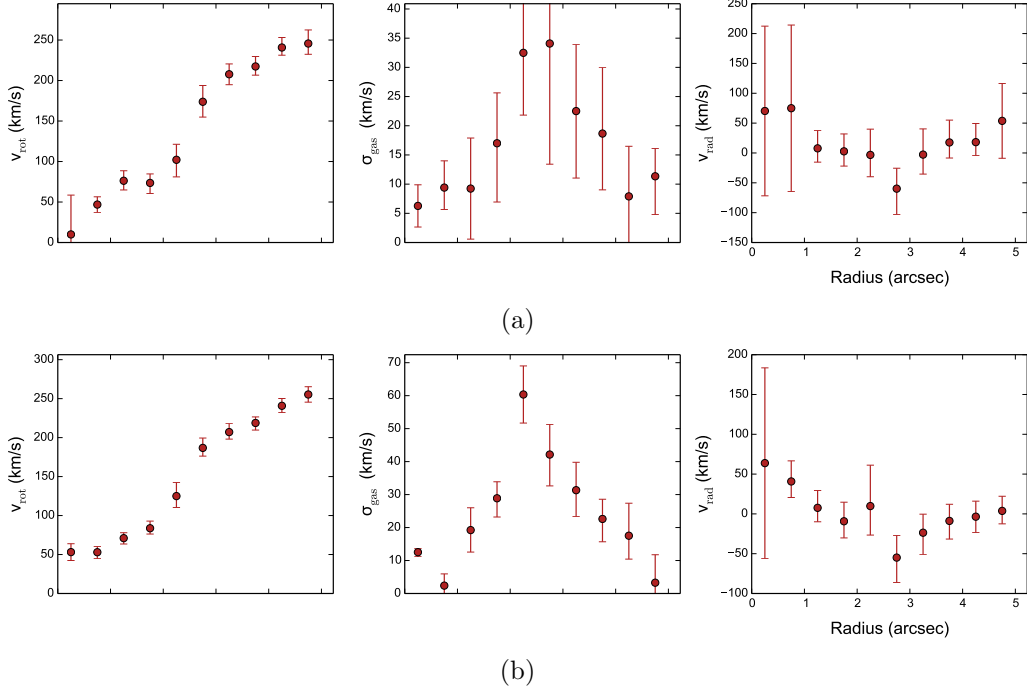


Figure 5.13: Parameters of the disk for the azimuthal (upper panels) and "local" (lower panels) non-circular models of 3D-Barolo.

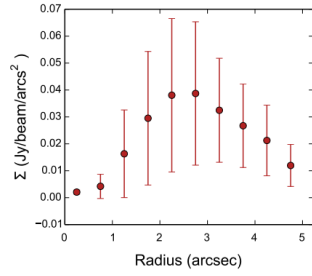


Figure 5.14: Surface brightness Σ produced by Barolo for all models.

3D-Barolo azimuthal rotational model

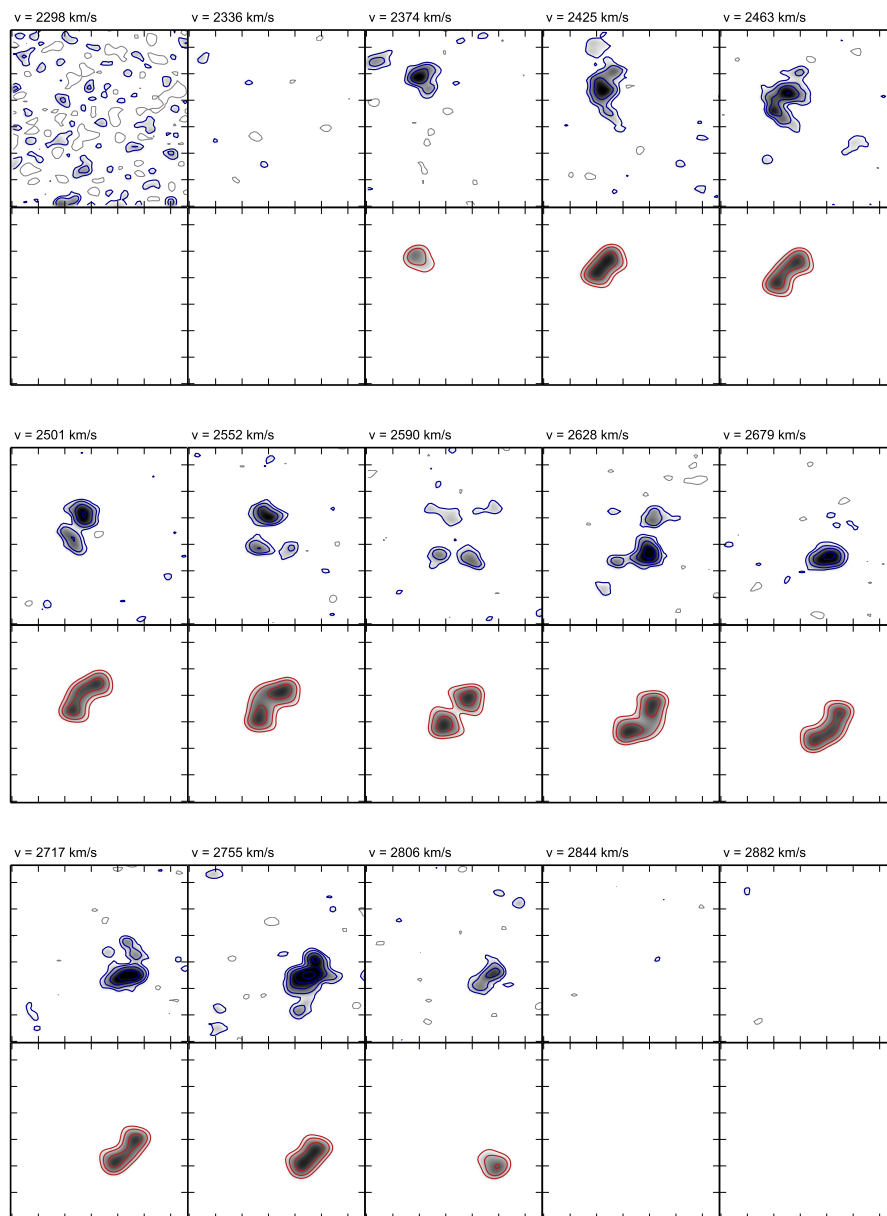


Figure 5.15: Comparison between the data (blue, top panels) and the azimuthal rotational model (red, bottom panels) in fifteen representative channel maps. The size of the field is $12'' \times 12''$. The lower contours start from 2.5σ , negative contours are shown in grey.

3D-Barolo local rotational model

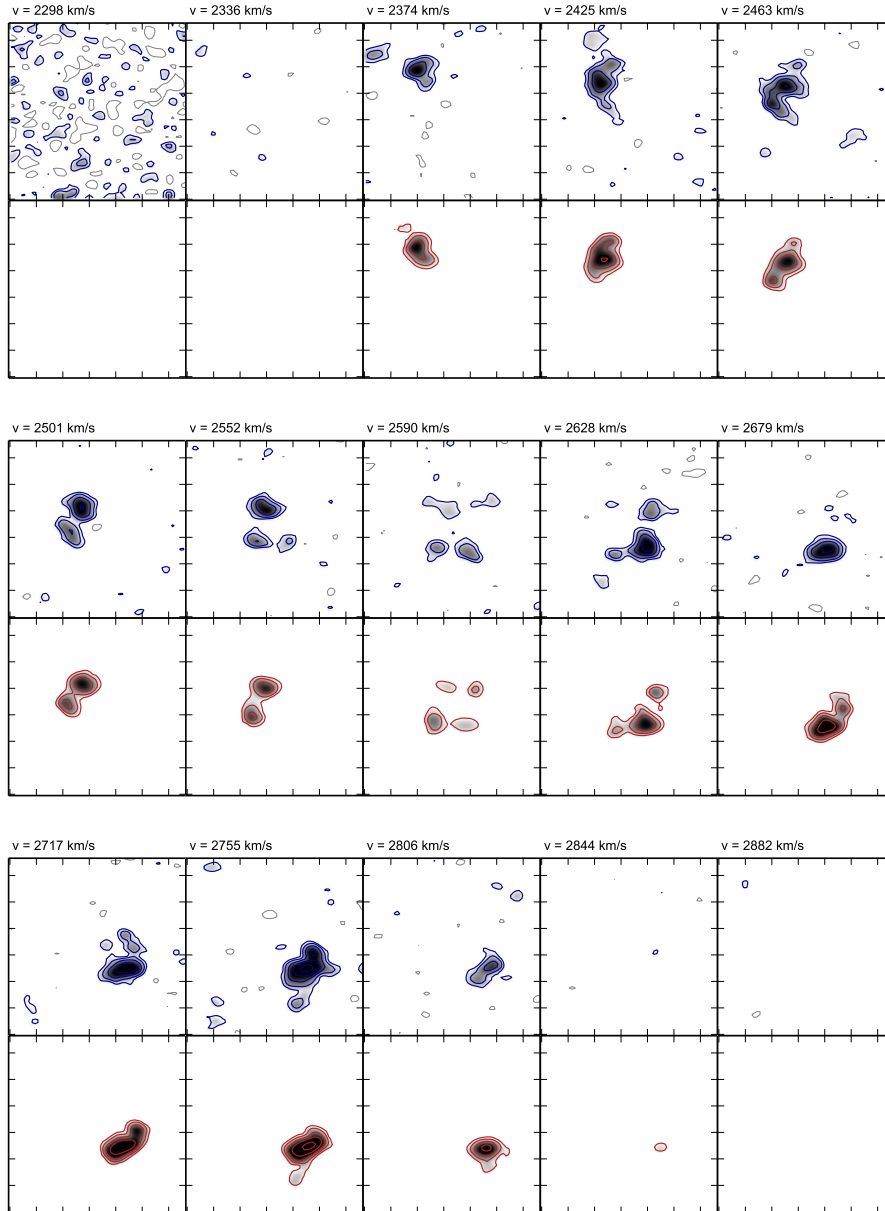


Figure 5.16: Comparison between the data (blue, top panels) and the local rotational model (red, bottom panels) in fifteen representative channel maps. The size of the field is $12'' \times 12''$. The lower contours start from 2.5σ , negative contours are shown in grey.

3D-Barolo azimuthal non-circular model

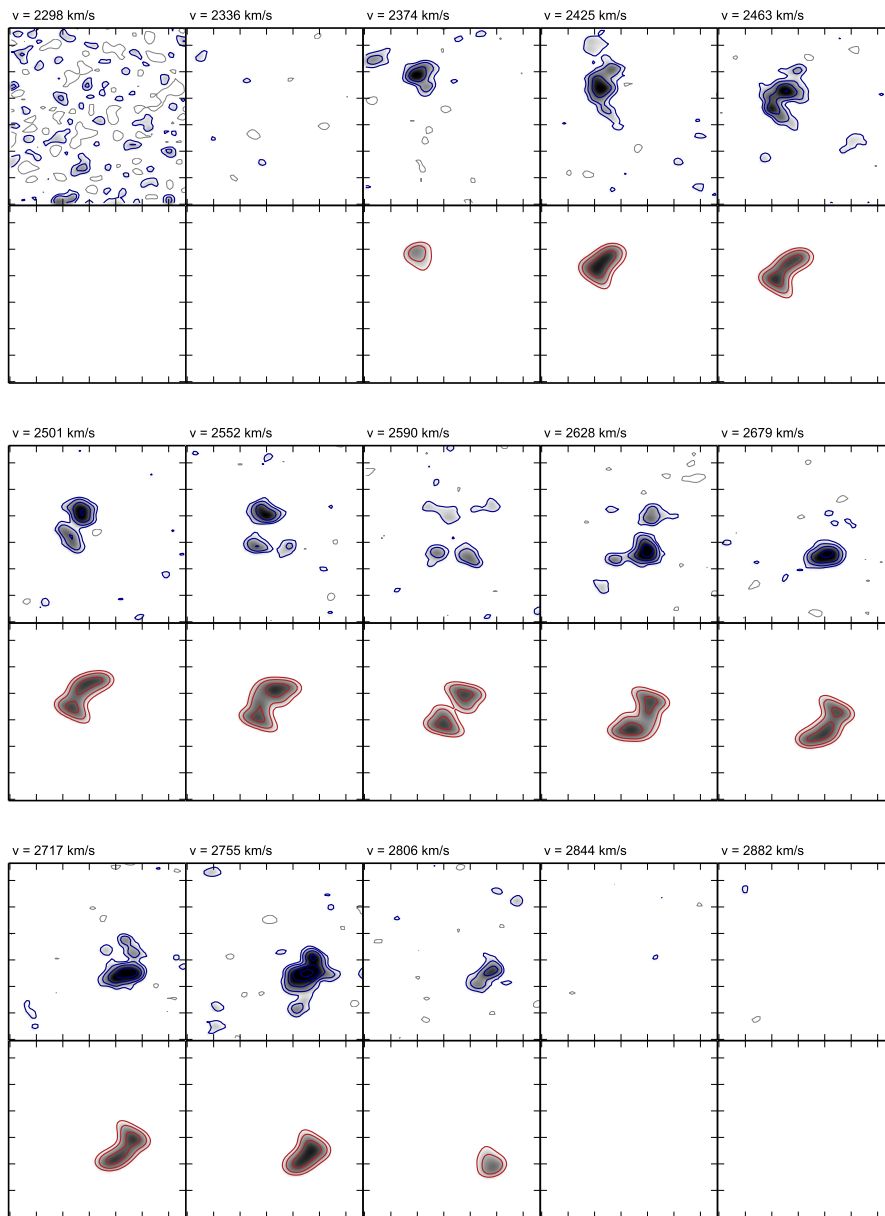


Figure 5.17: Comparison between the data (blue, top panels) and the azimuthal non-circular model (red, bottom panels) in fifteen representative channel maps. The size of the field is 12'' x 12''. The lower contours start from 2.5σ , negative contours are shown in grey.

3D-Barolo local non-circular model

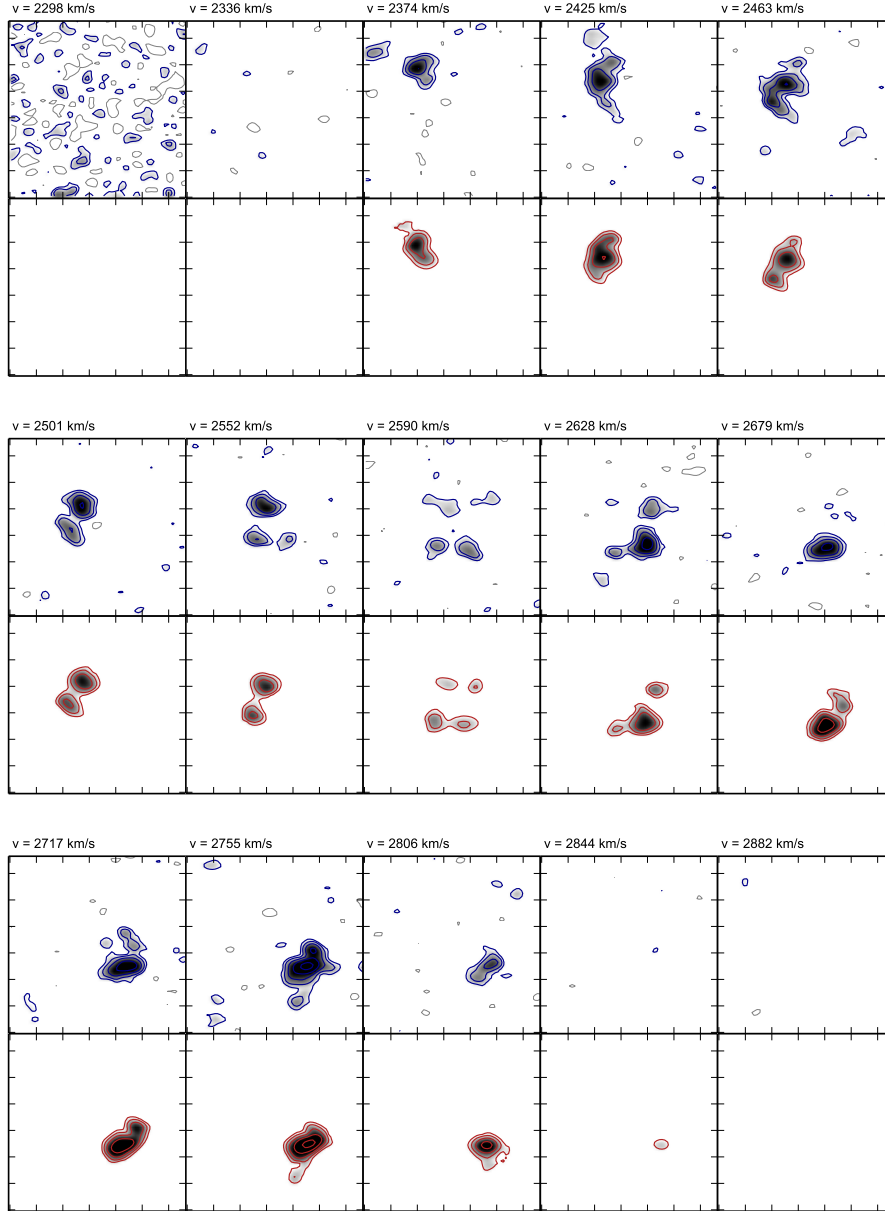


Figure 5.18: Comparison between the data (blue, top panels) and the local non-circular model (red, bottom panels) in fifteen representative channel maps. The size of the field is $12'' \times 12''$. The lower contours start from 2.5σ , negative contours are shown in grey.

Finally, Figures 5.19 - 5.22 show the PV diagrams obtained for the two models and the two normalizations. Again local normalization better represent the data by construction. We notice that Barolo better reproduces the inner regions of the PV diagram along the major axis than TiRiFiC. On the other hands, as TiRiFiC, it tends to provide a poor fit to the data along the minor axis. Also Barolo non-circular model is able to produce a tilt in the PV diagram along the minor axis, but this tilt is less evident than the one produced by the Tirific non circular model, which provides a much better fit to the data.

3D-Barolo azimuthal rotational model

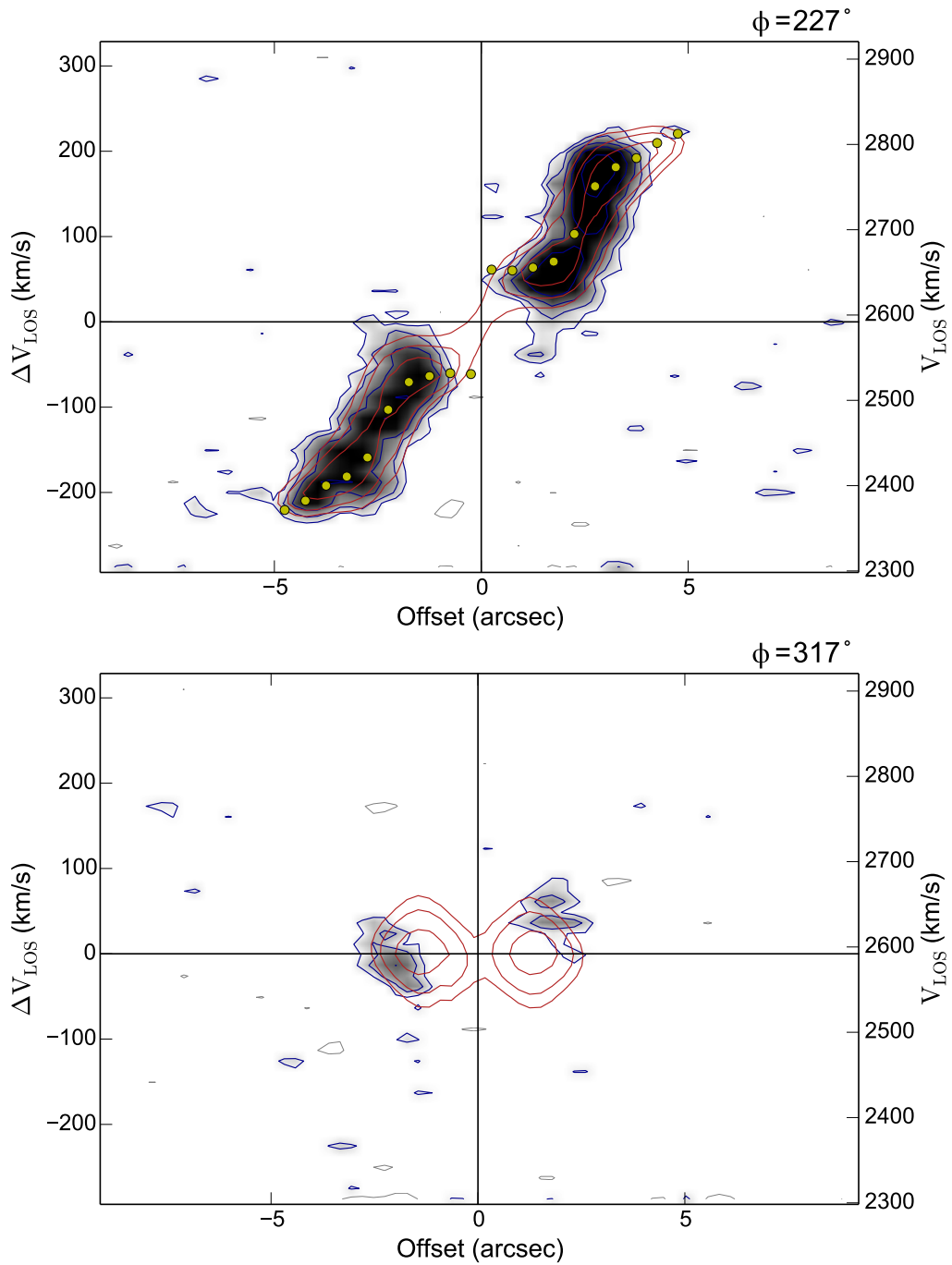


Figure 5.19: Position-velocity diagrams along major (top) and minor (bottom) axes for the azimuthal rotational model. Data are shown in grey-scale with blue contours, models in red, rotation curves as yellow dots.

3D-Barolo local rotational model

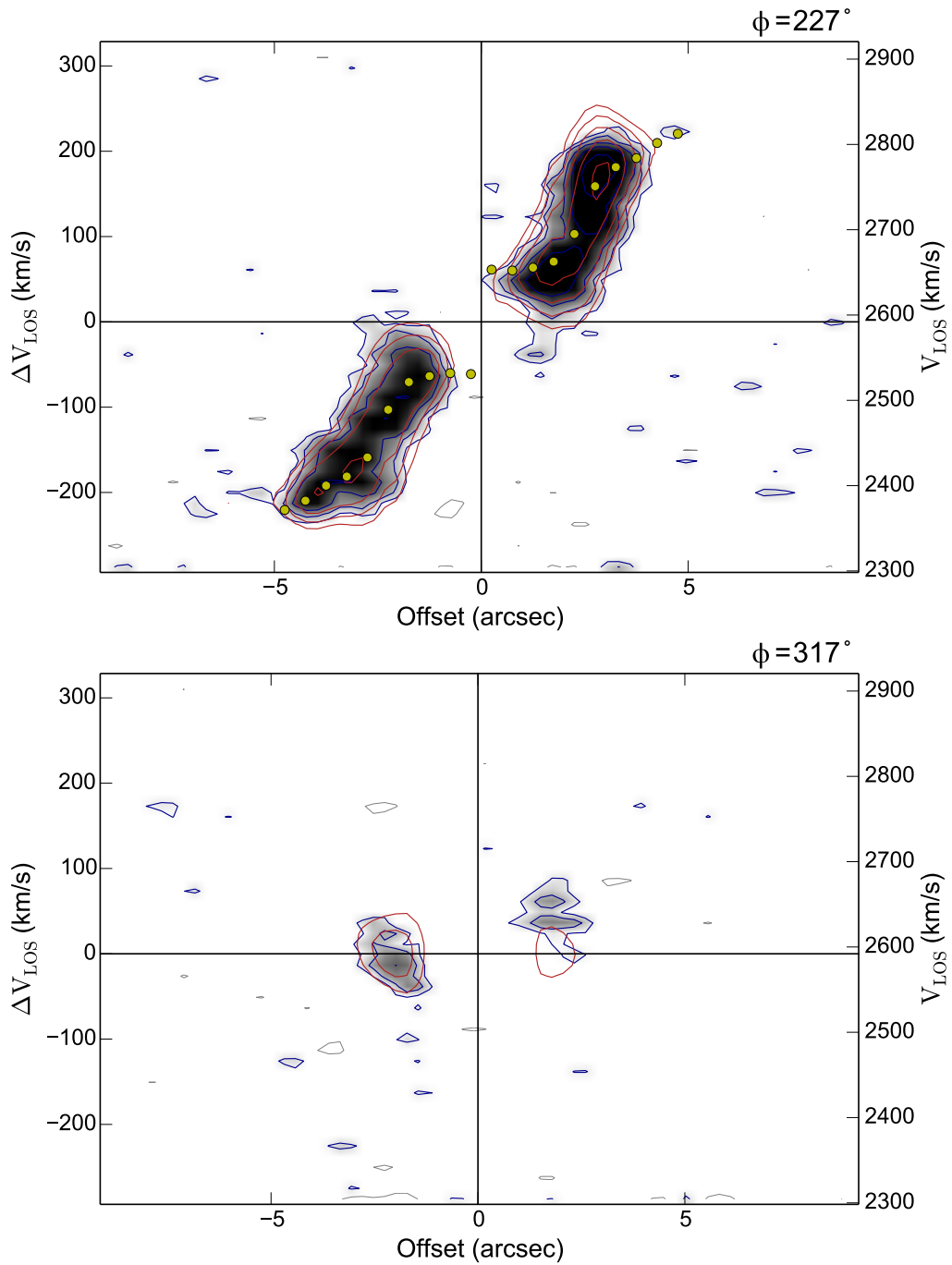


Figure 5.20: Position-velocity diagrams along major (top) and minor (bottom) axes for the local rotational model. Data are shown in grey-scale with blue contours, models in red, rotation curves as yellow dots.

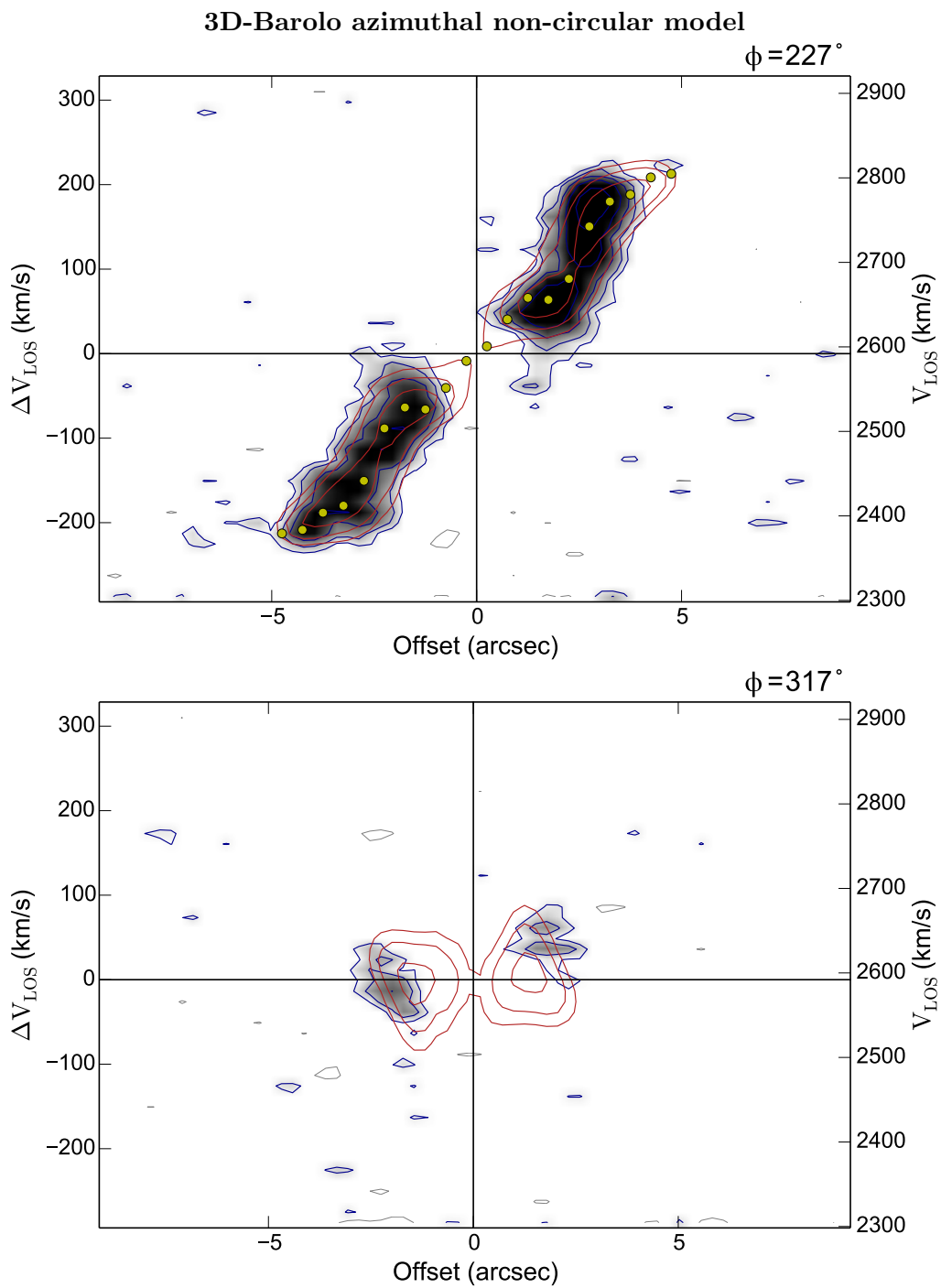


Figure 5.21: Position-velocity diagrams along major (top) and minor (bottom) axes for the azimuthal non-circular model. Data are shown in grey-scale with blue contours, models in red, rotation curves as yellow dots.

3D-Barolo local non-circular model

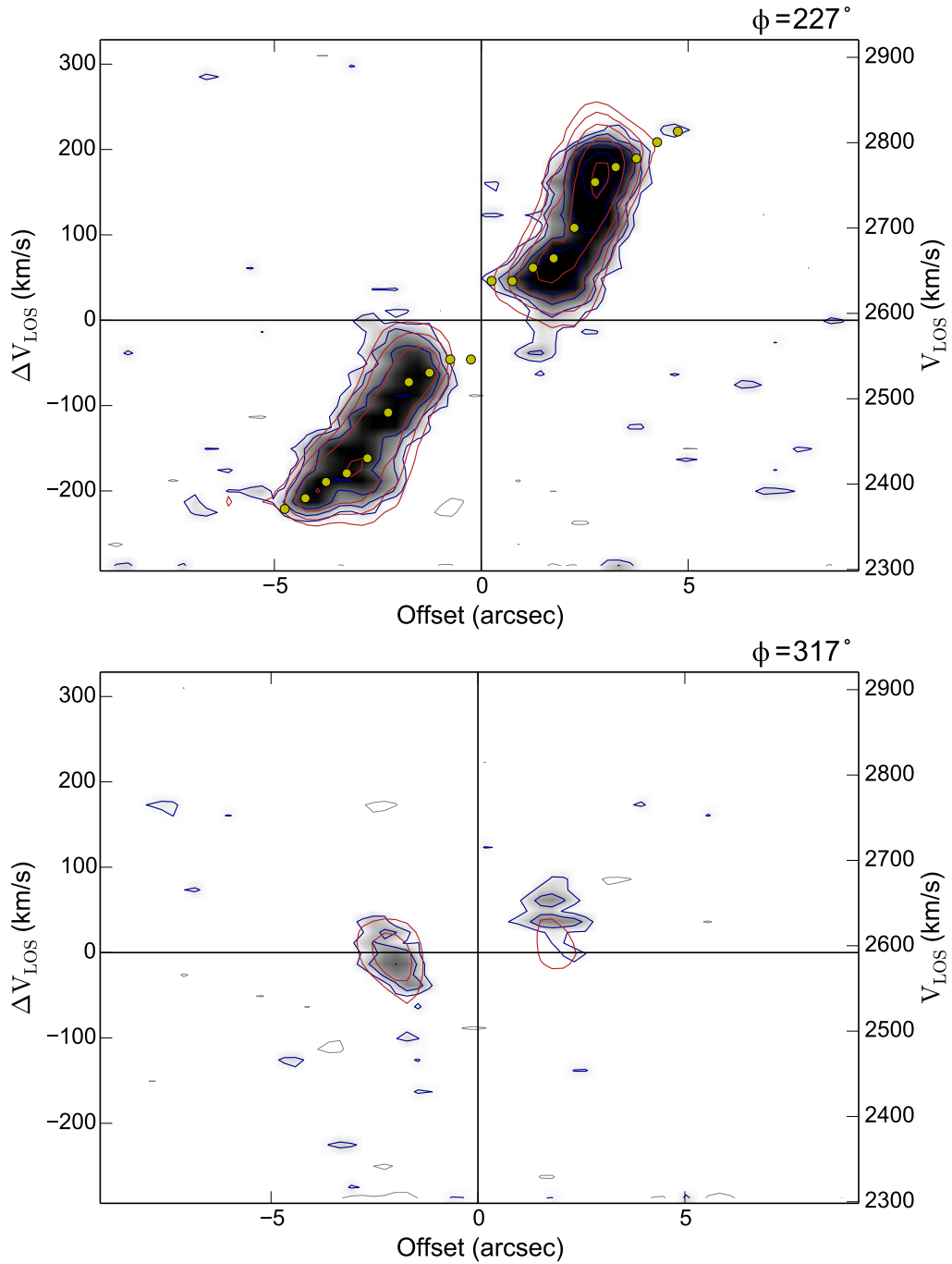


Figure 5.22: Position-velocity diagrams along major (top) and minor (bottom) axes for the local non-circular model. Data are shown in grey-scale with blue contours, models in red, rotation curves as yellow dots.

5.2.4 TiRiFiC and 3D Barolo: Moment 1 maps and rotation curves

A direct comparison between data and moments 1 maps of the models could help to further constrain the presence of non-circular motions in NGC 3100.

Figure 5.23 shows the moments 1 of the TiRiFiC rotational and non-circular models.

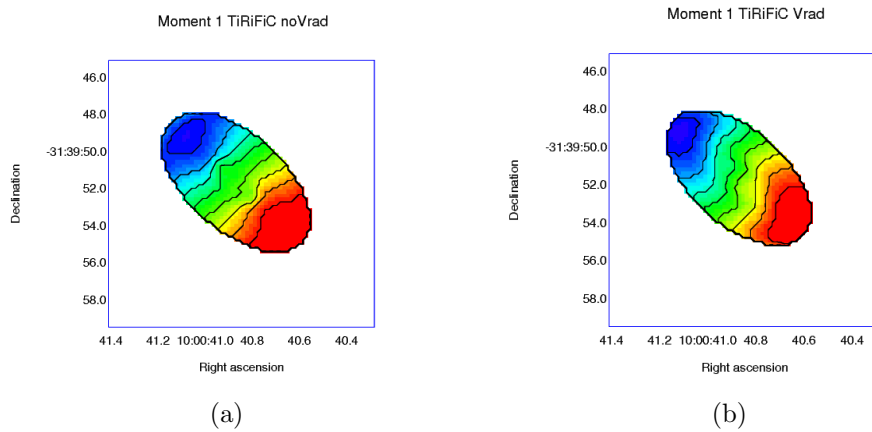


Figure 5.23: Integrated velocity maps (moments 1) of TiRiFiC (a) rotational and (b) non-circular models. Contours from $V = 2300 \text{ km/s}$ to $V = 2726 \text{ km/s}$ with $V_{sys} = 2592 \text{ km/s}$.

Figure 5.24 and 5.25 show the moment 1 maps of the two models obtained with Barolo for azimuthal and local normalization respectively. In all cases, the non-circular models seem to better reproduce the tilt present in the observed velocity field (See Figure 5.6).

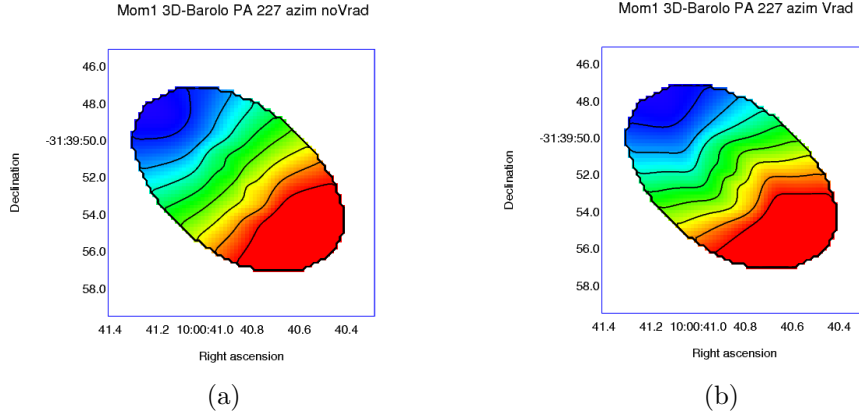


Figure 5.24: Integrated velocity maps (moments 1) of azimuthal (a) rotational and (b) non-circular 3D-Barolo models. Contours from $V = 2300 \text{ km/s}$ to $V = 2726 \text{ km/s}$ with $V_{sys} = 2592 \text{ km/s}$.

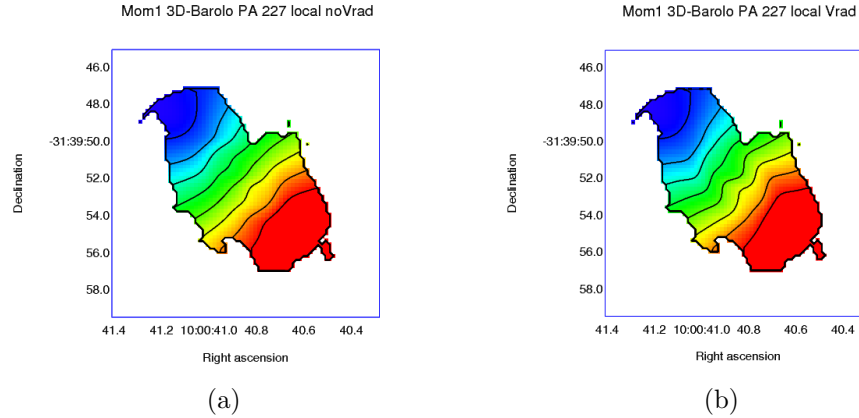


Figure 5.25: Integrated velocity maps (moments 1) of local (a) rotational and (b) non-circular 3D-Barolo models. Contours start from $V = 2300 \text{ km/s}$ to $V = 2726 \text{ km/s}$ with $V_{sys} = 2592 \text{ km/s}$.

Another interesting indication pointing towards a complex velocity field comes from the analysis of the rotation curves, that are presented again in Figure 5.26 (for the non-circular models only). In this case the full rotation curve is shown, and not only half of it (as in the previous plots). The reported flattening at $r < 2 \text{ arcsec}$ can be interpreted also as a local ($r \sim 2 \text{ arcsec}$) drop in velocity with respect to the expected value for regular rotation. We can speculate that this drop corresponds to an in-/out-flow. Alternatively we may have a two-disk system, with the inner one showing a different position

angle from the larger. Unfortunately the emission is very weak in the tilted region, and firm conclusions cannot be drawn.

TiRiFiC and 3D-Barolo (azimuthal non-circular model) rotation curves

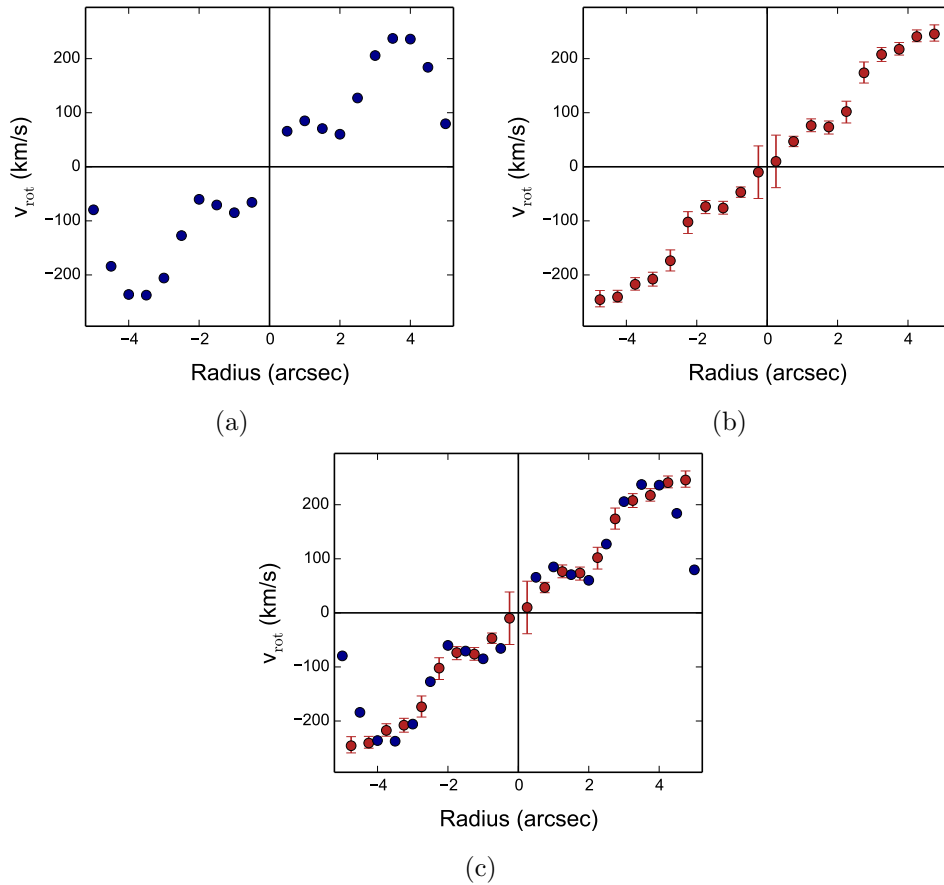


Figure 5.26: Rotation curve from (a) TiRiFiC (in blue) and (b) 3D-Barolo (in red) non-circular models. For 3D-Barolo it is considered the azimuthal non-circular model. TiRiFiC has no error bars. (c) Rotation curves from TiRiFiC (blue) and 3D-Barolo (red) overlapped.

Conclusions

This thesis is part of a project aimed at providing a comprehensive study of different galaxy components (stars, warm, cold gas) in the core of radio-loud early-type galaxies, and look for kinematical signatures of feeding/feedback loops that can be causally related to the presence of radio jets. For this purpose a complete, volume limited ($z < 0.03$) sample of eleven radio galaxies in the Southern sky was selected from the Parkes 2.7-GHz survey. This sample is the target of VLT/VIMOS integral-field-unit optical spectroscopy (warm gas and stellar components) and ALMA CO line imaging (molecular gas). This thesis inquired into the kinematics of molecular gas in the centre of one of the sources in the sample: NGC 3100, a FRI radio galaxy hosted by a S0 galaxy at redshift $z = 0.0088$.

NGC 3100 was observed with APEX at 230 GHz and showed a CO(2-1) line profile (double-horned) consistent with the presence of a rotating disk (Laing et al. in prep). The inner region of NGC 3100 was then imaged with ALMA at Band 6 during Cycle 3.

In this thesis, ALMA data was reduced and a data cube was obtained with a beam of $1.01 \times 0.73 \text{ arcsec}^2$, where a CO(2-1) 230-GHz line was clearly detected. The line is organized in a disk/ring-like rotating structure with some surrounding clumps.

The ALMA radio continuum data, on the other hand, revealed the inner part of the radio jets, entirely consistent with those imaged at similar resolution with the VLA at 5 GHz and 8.5 GHz. A full analysis of the CO(2-1) line emission was made through the integrated intensity map (*moment 0*) and the integrated velocity map (*moment 1*). The mass of the molecular gas resulted in $M = 1.85 \pm 0.4 \times 10^8 M_{\odot}$, consistent with what found with APEX. The CO map was compared with the distribution of dust (from B-I absorption image) in the inner region of the host galaxy. A nice overlap was found for the structures detected in both images.

The molecular gas disk shows a complex kinematics, which can suggest the presence of non-circular motions and/or warps (i.e. variations of position angle) in the disk.

Two programs were used to model the disk: *TiRiFiC* and *3D-Barolo*. Both purely rotational models and models including non-circular motions were explored. Different models of the gas disk with different fixed position angles and inclinations were produced. The position angle that best reproduces the whole structure is 227° . The best-fit inclination resulted in 60° . The purely rotational models produced disks with rotational velocity in a range of $\sim \pm 200 \text{ km/s}$, consistent with the data. Non-circular models seem to better reproduce some of the data features (tilts in the moment 1 and PV diagrams), but do not provide a clear estimate of the radial velocity, which is consistent with a zero value at all radii, except around 3 arcsec, where a value of $\sim 50 \text{ km/s}$ is estimated.

TiRiFiC and *3D-Barolo* models generally show consistent results. Unfortunately the emission is very weak in the inner region, where the tilt in the velocity field is seen, and firm conclusions cannot be drawn. In addition, there is a degeneracy between non-circular motions and warps, so the observed features could be in principle reproduced by warped disks, i.e. allowing the position angle to vary along the disk, rather than through the inclusion of non-circular motions.

We plan to further investigate this latter hypothesis in the next future.

Bibliography

- [1] Alatalo K., Davis T. A., Bureau M., et al., 2013, MNRAS, 432, 1796
- [2] Allen, S. W., Dunn, R. J. H., Fabian, A. C., Taylor, G. B., and Reynolds, C. S., 2006, MNRAS, 372, 21
- [3] Antonucci R., 1993, ARA&A, 31, 473
- [4] Baldwin J. A., Phillips M. M., Terlevich R., 1981, PASP, 93, 5
- [5] Bettoni D., Falomo R., Fasano G., Govoni F., Salvo M., Scarpa R., 2001, A&A, 380, 471
- [6] Bolatto A. D., Wolfire M. & Leroy A. K., 2013, ARA&A, 51, 207
- [7] Bondi H., 1952, MNRAS, 112, 195
- [8] Buttiglione S., Capetti A., Celotti A., Axon D. J., Chiaberge M., Macchetto F. D., Sparks W. B., 2010, W. B., 2010, A&A, 509, 6
- [9] Cappellari M., et al., 2011, MNRAS, 416, 1680
- [10] Cappellari M., et al., 2011, MNRAS, 413, 813
- [11] *CASA Synthesis & Single Dish Reduction, Reference Manual & Cookbook*, V. April 11, 2016, NRAO
- [12] Carilli C. L. & Walter F., 2013, ARA&A, 51, 105
- [13] Colbert James W., Mulchaey John S., Zabludoff Ann I., 2001, AJ, 121, 808
- [14] Davies T., et al., 2011, MNRAS, 417, 882

- [15] de Ruiter H. R., Parma P., Capetti A., Fanti R. & Morganti R., 2002, *A&A*, 396, 857
- [16] Di Teodoro E. M., Fraternali F., 2015, *MNRAS*, 451, 3021
- [17] Dopita M. A., Shastri P., Davies R., Kewley L., et al., 2015, *ApJ. Suppl. Series*, 217, 12
- [18] Ekers R. D., Wall J. V., Shaver P. A., Goss W. M., Fosbury R. A. E., Danziger I. J., Moorwood A. F. M., Malin D. F., Monk A. S., Ekers J. A., 1989, *MNRAS*, 236, 737
- [19] Emsellem E., et al., 2004, *MNRAS*, 352, 721
- [20] Faber S. M., et al., 2007, *ApJ*, 665, 265
- [21] Fabian A. C., 2012, *ARA&A*, 50, 455
- [22] Fanaroff B. L., Riley J. M., 1974, *MNRAS*, 167, 31
- [23] Gaspari M., Ruszkowski M., & Oh S. P., 2013, *MNRAS*, 432, 3401
- [24] Govoni F., Falomo R., Fasano G. & Scarpa R., 2000, *A&AS*, 143, 369
- [25] Hardcastle M. J., Evans D. A. & Croston J. H., 2007, *MNRAS* 376, 1849
- [26] Heckman T. M. & Best P. N., 2014, *ARA&A*, 52, 589
- [27] Horellou C., Black J. H., van Gorkom J. H., et al., 2001, *A&A*, 376, 837
- [28] Józsa G. I. G., Kenn F., Klein U., Oosterloo T. A., 2007, *A&A*, 468, 731
- [29] Kauffmann G., Heckman T. M., Tremonti C., et al., 2003, *MNRAS*, 346, 1055
- [30] Kewley L. J., Dopita M. A., Sutherland R. S., Heisler C. A., Trevena J., 2001, *ApJ*, 556, 121
- [31] Kewley L. J., Groves B., Kauffmann G., Heckman T., 2006, *MNRAS*, 372, 961

- [32] Laing R. A., Jenkins C. R., Wall J. V., Unger S. W., 1994, in *The First Stromlo Symposium: The Physics of Active Galaxies.*, eds. G.V. Bicknell, M.A. Dopita, and P.J. Quinn, ASP Conference Series, 54, 201
- [33] Lauer T. R., Faber S. M., Gebhardt K., et al., 2005, AJ, 129,2138
- [34] Lelli F., Verheijen M., Fraternali F., Sancisi R., 2012, A&A, 537, A72
- [35] Leon S., Lim J., Combes F. & Dinh-v-Trung., 2003, in Astronomical Society of the Pacific Conference Series, Vol. 290, *Active Galactic Nuclei: From Central Engine to Host Galaxy*, ed. S. Collin, F. Combes, & I. Shlosman,525
- [36] Lim J., Leon S., Combes F. & Dinh-v-Trung. 2003, in Astronomical Society of the Pacific Conference Series, Vol. 290, *Active Galactic Nuclei: From Central Engine to Host Galaxy*, ed. S. Collin, F. Combes, & I. Shlosman, 529
- [37] Ocaña Flaquer B., Leon S., Combes F. & Lim J., 2010, A&A, 518, A9
- [38] Okuda T., Kohno K., Iguchi S. & Nakanishi K., 2005, ApJ, 620, 673
- [39] Oser L., Ostriker J.P., Naab T., Johansson P.H., Burkert A., 2010, ApJ, 725, 2312
- [40] Pizzolato F. & Soker N., 2005, ApJ, 632, 821
- [41] Prandoni I., Laing R. A., de Ruiter H. R. & Parma P., 2010,A&A, 523, A38
- [42] Prandoni I., Laing R. A., Parma P., et al., 2007, New A Rev., 51, 43
- [43] Remijan A., et al., 2015, *ALMA Cycle 3 Technical Handbook Version 1.0*, ALMA Partnership
- [44] Rogstad D. H., Lockhart I. A., Wright M. C. H., 1974, ApJ, 193, 309
- [45] Rogstad D. H., Shostak G. S., 1971, A&A, 13, 99

- [46] Russell H. R., McNamara B. R., Edge A. C., et al., 2013, MNRAS, 432, 530
- [47] Salim S., et al., 2007, ApJ. Suppl. Series, 173, 267
- [48] Sandage A., Brucato R., 1979, AJ, 84, 472
- [49] Schmidt P., Józsa G. I. G., et al., 2014, A&A, 561, A28
- [50] Solomon P. M. & Vanden Bout P. A., 2005, ARA&A, 43, 677
- [51] Urry C. M., Padovani P., 1995, PASP, 107, 803
- [52] York D. G., et al., 2000, AJ, 120, 1579
- [53] Young L. M., et al., 2011, MNRAS, 414, 940Y